Journal of Constructional Steel Research 245 (2026) 110510

Contents lists available at ScienceDirect

Journal of Constructional Steel Research

journal homepage: www.elsevier.com/locate/jcsr

Novel additively manufactured connections for cold-formed steel construction: FE investigation

Ehsan Bakhshivand [a,*], Chuandong Xie [a], Ornella Iuorio [b], Francesca Paradiso [c], Barbara Previtali [c], Alireza Bagheri Sabbagh [a]

[a] School of Engineering, University of Aberdeen, Aberdeen, AB24 3FX, UK
[b] Department of Architecture, Built Environment and Construction Engineering, Politecnico di Milano, Milan, 20133, Italy
[c] Department of Mechanical Engineering, Politecnico di Milano, Milan, 20156, Italy

ARTICLE INFO

Dataset link: ADDLIGHTS concept study

Keywords:
Cold-formed steel
Metal additive manufacturing
Interlocking connection
Lightweight steel framing
LMD
WAAM

ABSTRACT

Within this study a hybrid lightweight steel framing (LSF) system is developed, integrating novel additively manufactured (AM) connections utilising wire and arc additive manufacturing (WAAM) and laser metal deposition (LMD). By means of validated finite element studies, the gravity and pushover response of the developed AM-LSF system is investigated and compared to that of conventional LSF systems. AM connections comprise multiple tooth wheel-shaped connectors printed on the LSF joist and stud members, creating an interlocking mechanism. The results indicate comparable gravity and pushover performance of the AM-LSF with that of the conventional LSF. A combined joist–stud–wheel yielding and local buckling of the joist around the wheel region is identified as the governing limit state, depending on the AM connection configurations, which affects the gravity and pushover performance of the frames. AM connection prototyping reveals practicality aspects of both WAAM and LMD printing methods. Beyond structural performance, the proposed AM-LSF system offers practical benefits including reduced on-site labour, faster construction, and potential for reuse and sustainable construction.

1. Introduction

The construction industry has a considerable environmental footprint, consuming around 60% of global resources and nearly 40% of global energy and is responsible for more than 25% global waste and 40% greenhouse gas emissions [1–4]. Therefore, it is crucial to devise novel structural design solutions to reduce material usage and waste while improving structural efficiency. Lightweight steel framing (LSF) structures made of cold-formed steel (CFS) sections are gaining increasing popularity in modern construction practices. They offer materially efficient and low-carbon structural systems, provide flexibility for tailored design solutions, and are scalable for technologies related to automated construction [5].

Figs. 1(a)–1(c) show three floor-to-wall construction methods employed for conventional LSF systems, including platform, balloon, and ledger framing systems. The platform framing, shown in Fig. 1(a), is the most traditional method with floor joists stacked on the wall studs which interrupt the vertical load path. In balloon framing, the floor joists are connected to the face of the walls with continuous studs over more than one storey, as shown in Fig. 1(b), rarely used due to erection difficulties. The ledger framing, with floor joists hung off the walls, shown in Fig. 1(c), is the current best-practice construction method, which can be considered as a combination of platform and balloon framing systems. These are all categorised as simply supported frames with low connection stiffness and are predominantly controlled by the joist mid-span deflection limit state, leading to relatively heavy and deep CFS joists to provide the required stiffness [6]. A recent experimental study [6] revealed various types of premature local failure limit states in the components of ledger-framed floor-to-wall connections, most notably stud web crippling. These occur primarily due to the imposed eccentricity and the consequential out-of-plane actions within the floor-to-wall connection.

To eliminate the out-of-plane actions within the connection components, a planar type of semi-rigid floor-to-wall connection (see Fig. 1(d)) has been recently developed [7], in which the floor joists are directly connected to the webs of studs using screw connections, without the need for additional steel angles, forming a side-framed lightweight steel (SFLS) system. This provides an in-plane load transferring mechanism within the floor-to-wall connection, thereby eliminating the localised failures typically observed in conventional systems. The proof of concept study conducted by [7] through FE investigation

* Corresponding author.
E-mail address: e.bakhshivand.23@abdn.ac.uk (E. Bakhshivand).

https://doi.org/10.1016/j.jcsr.2026.110510
Received 3 December 2025; Received in revised form 27 April 2026; Accepted 3 June 2026
Available online 11 June 2026

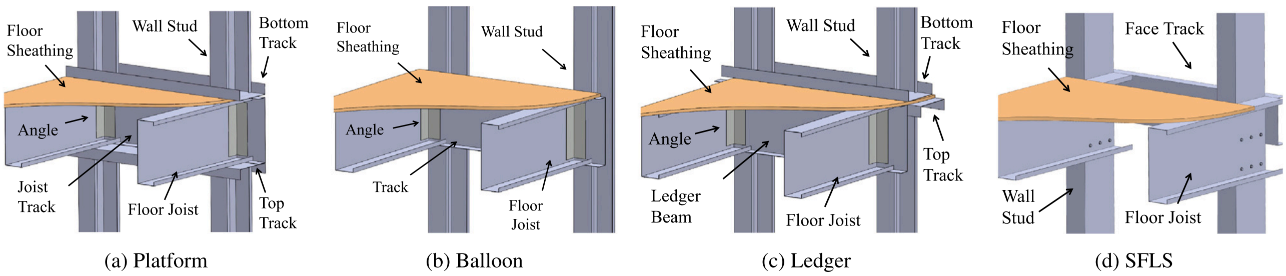

Fig. 1. CFS framing options.

demonstrated that the proposed SFLS system can result in a 28% lighter floor joist and a more efficient LSF system with fewer framing members and connections.

As the construction industry seeks more efficient, automated, and reusable building solutions, additive manufacturing (AM) can be employed to advance conventional construction methods in LSF systems. Compared to conventional production methods, AM presents several advantages, including advanced automation, geometric flexibility, off-site manufacturing, greater worker safety through the reduction of on-site repetitive labor work, along with potential opportunities for repair and strengthening [8–10]. To leverage these capabilities within the construction industry, AM has been increasingly utilised for producing a diverse array of objects. These range from intricately optimised small-scale components to large-scale construction purposes [11–14].

Among the various types of AM technology outlined in ISO/ASTM 52900 [15], powder bed fusion (PBF) and directed energy deposition (DED) are particularly promising for the steel construction industry due to their ability to produce complex geometries suitable for architectural and engineering designs [16]. While PBF excels in creating intricate, high-quality parts, its slow deposition rate and limited build size hinder its application in construction. DED, including laser-powder, laser-wire, electron beam-wire, and arc-wire processes, offers a broader spectrum of capabilities. Wire and arc additive manufacturing (WAAM), in particular, has become popular for making structural parts due to its cost-effectiveness, high deposition rate, and large build size [14]. However, it compromises on dimensional accuracy and surface quality compared to the other DED methods. Laser metal deposition (LMD), on the other hand, delivers superior part finish and precision at the expense of higher costs, lower efficiency, and smaller build volumes [17].

Over recent years, an increasing number of investigations have been undertaken to provide a clear understanding of the material, cross-sectional, and structural behaviour of metal AM products for structural purposes and to foster more widespread use of AM in steel construction [13,14,18–23]. Further investigations also demonstrated the applicability of AM technology in the manufacturing of steel connections [24–27]. These studies showed that by applying the advantages and versatility of AM in printing complex geometries, conventional labour-intensive connections can be either replicated with faster or completely new, optimised geometries. Additionally, a recent review on hybrid manufacturing approaches combining additively manufactured components with conventional steel structures highlights the growing potential of such systems to enhance geometric freedom, streamline fabrication, and improve structural performance, showing the need for further research in this area [28].

Building on the capabilities of AM, the present study proposes a hybrid LSF system featuring a novel, fastener-free, additively manufactured connecting method. This has been designed as an alternative to traditional bolted or screw connections, which typically require considerable time and effort to implement. Practical AM connection configurations are first developed, followed by a comprehensive finite element (FE) investigation, supported by structural-level validation, to assess the gravity and pushover performance of the proposed AM-LSF system. The effects of construction method, printing technique, and connector geometrical parameters are evaluated and compared with the conventional system with screw connections. Finally, sample prototyping has been conducted to identify the potential manufacturing challenges of the developed AM connections.

2. AM connection configurations for LSF

Fig. 2(a) shows two male and female connectors in the shape of matching wheels, directly manufactured on the webs of a joist and a stud using DED-based AM processes, forming a novel type of connection called the gear-wheel (GW) connection. As an alternative to the GW connection, the wheel can be fitted into a matched hole (see Fig. 2(b)), forming a key-wheel (KW) connection which has been developed by the authors in companion research. Thanks to the design freedom provided by AM processes and the resulting manufacturing flexibility, the considered configuration can be a wide range of shapes comprising multiple teeth for interlocking purposes, as shown in Fig. 2(c), forming a semi-rigid type of connection. The key variables include diameter, number of teeth, tooth depth, thickness, and wheel depth.

As illustrated in Fig. 2(a) and 2(b), the assembly of the connections is achieved through gravity-based placement and sliding: either by inserting the wheels into one another in the GW configuration, or by fitting the wheel into the matching hole in the KW configuration. This creates an interlocking connection that resists the shear force and bending moment of the connection through the bearing surfaces of the wheel teeth. Note that the interlocking load path places the shear demand close to the shear centre of the C-shaped CFS joist and stud, thereby limiting unfavourable effects associated with load eccentricity. During the construction stage, temporary stability of the interlocking connection is ensured by the self-weight of the joist-stud assembly together with standard site clamping used during placement and alignment. After installation, the separation is prevented by the restraining effects provided by the floor and wall sheathing, which act together with the interlocking engagement of the connector teeth.

The AM-LSF system developed herein is intended for floor–wall framing systems in CFS buildings, which are used in residential and light commercial construction. Compared to conventional LSF systems, this system can potentially provide design and manufacturing flexibility, faster construction, improved quality due to reduced manual operations, and ease of dismantling and non-destructive deconstruction, which facilitates future adaptations and reuse. Although the AM-LSF system may involve higher upfront manufacturing costs than conventional systems with screw connections, its mentioned whole-life advantages can offset these initial expenses.

3. Design considerations and frame specifications

Fig. 3 shows two frame models which were selected from [7] and modified in terms of geometry and the number of stories to represent the sequential and continuous construction methods (SCM and CCM) of the LSF system. In SCM (see Fig. 3(a)), where studs are assembled one storey at a time, the full length of the studs was modelled. In CCM (shown in Fig. 3(b)), where studs span continuously over two storeys,

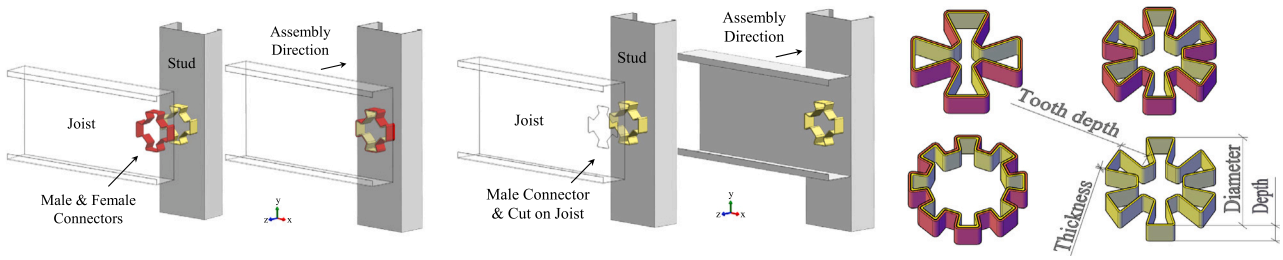

(a) GW connection (b) KW connection (c) Wheel geometrical properties

Fig. 2. Proposed interlocking connection configurations for the AM-LSF system.

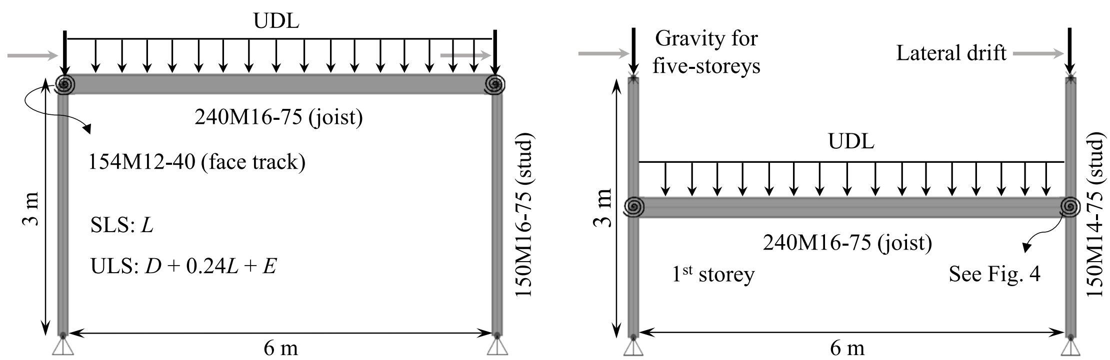

(a) SCM (b) CCM

Fig. 3. Frame models for SCM and CCM.

half-height studs from two consecutive floors were adopted, representing their inflection points under lateral loading. Both configurations had a clear span of 6 m and a storey height of 3 m. These frames represent the ground floor of a six-story residential building, repeated every 600 mm on-center. The studs were modelled as pinned at the base and restrained against out-of-plane movement at their tops. To better reflect common assembly practices, the effect of floor and wall sheathing on joists and studs has been considered, as this is expected to affect the structural performance of both the connections and the frames.

The dead load (D) of 1 $^{kN}/_{m^2}$ and the live loads (L) of 2 $^{kN}/_{m^2}$ and 1 $^{kN}/_{m^2}$ were applied to the floors and the roof, respectively, according to [29]. These values, applied as uniform distributed loads (UDL) together with the lateral load (E) in terms of pushover drift, were incorporated into two loading scenarios, representing the serviceability limit state (SLS) and the ultimate limit state (ULS). The relevant load combinations and associated partial factors, adopted from [29,30], are shown in Fig. 3(a). The gravity loads from the upper floors were applied to the studs via point loads, whereas those on the first floor were uniformly distributed on the joist. Fig. 4(a) shows the cross-sections of the CFS members used in the study. The joist section was 240M16–75 for both SCM and CCM, while the stud sections were 150M16–75 and 150M14–75 for SCM and CCM, respectively. The section labels begin with the depth of web, followed by the thickness of section (without a decimal point), and conclude with the width of flange, all in millimeters. Both the joist and the stud were channel sections featuring 15 mm lips. Note that the member sections for each construction method were designed based on different screw patterns using the procedure presented in [7], and the governing (maximum) section sizes were conservatively adopted across all connection types to ensure a consistent basis for comparison.

For each of SCM and CCM, three types of screw, GW and KW connection configurations were considered for comparative purposes as shown in Figs. 4(b) and 4(c). For screw connections, one, three, and five lines of three #12 screws (with 5.4 mm diameter) were considered, while for GW and KW various circular and multi-tooth patterns were adopted, representing pin and semi-rigid connections. The number of teeth ranged from 4 to 8, with tooth depths of 20 mm and 40 mm, wheel thicknesses of 1.5 mm and 2 mm, and a wheel depth of 30 mm, manufactured using LMD and WAAM feedstock materials.

To clearly identify the different connection configurations, a labelling system was adopted. Screw connections are denoted by the letter “S”, followed by either “S” or “C” to indicate SCM and CCM, respectively, and then a digit representing the number of screw lines (e.g., SS-1, SC-3, SC-5). AM connections begin with “G” for GW or “K” for KW connections, followed by “S” or “C” to denote SCM or CCM, and “W” or “L” to indicate the manufacturing method, WAAM or LMD, respectively. The label concludes with a numeric part, indicating number of teeth, tooth depth (mm), and tooth thickness (mm×10). For example, GCW-8-20-20 refers to a GW connection with CCM, manufactured using WAAM, featuring wheels with 8-tooth, 20 mm tooth depth, and 2 mm thickness.

4. Finite element modelling

Within this section, the key features of the computational models, using the FE software Abaqus [31], have been presented, along with the validation results conducted using available experimental data in the literature and two physical tests of the AM-LSF system.

4.1. Material modelling

4.1.1. Cold-formed steel and sheathing board

The full stress–strain response of CFS steel, capturing its rounded yield plateau and subsequent gradual hardening, has been input into FE models using the constitutive model proposed by Gardner and Yun [32] based on S450 steel.

Oriented strand board (OSB) with thicknesses of 18 mm and 11 mm was considered for the floor and wall sheathings, respectively. Its

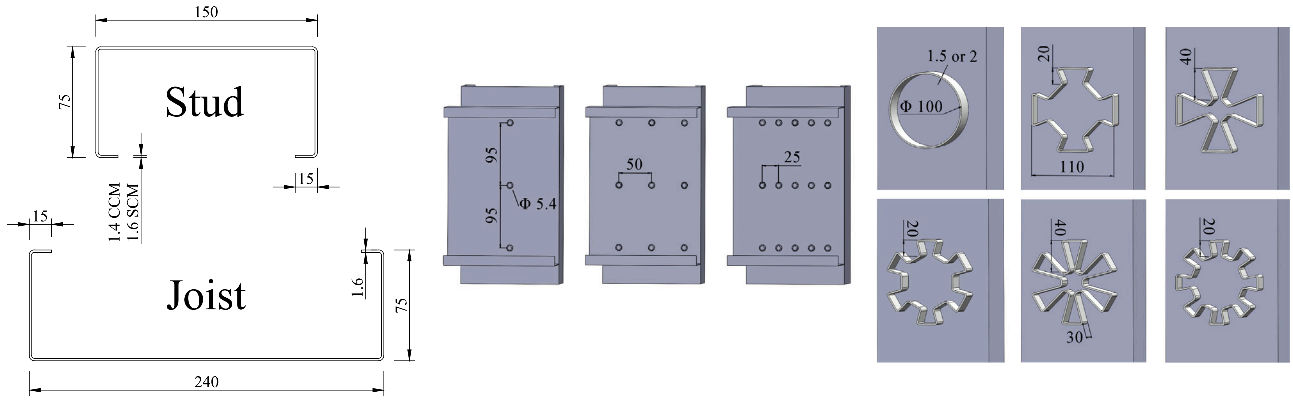

(a) Cross section properties (b) Screwed web (c) GW and KW

Fig. 4. Cross-sections of the CFS members and connection configurations (all dimensions in mm).

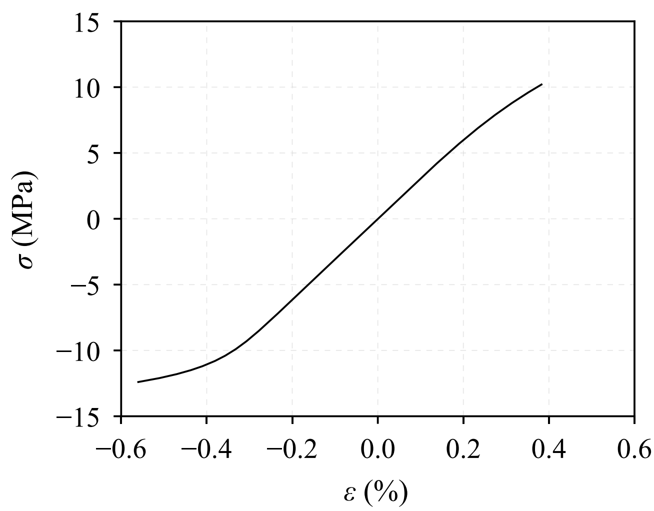

Fig. 5. Stress–strain response of the OSB material.

Table 1
Mechanical properties of OSB material.

E (MPa)	v	Tension			Compression		
		f_u (MPa)	ε_u (%)	n	f_u (MPa)	ε_u (%)	n
3080	0.2	10.2	0.38	4.1	12.4	0.56	12

stress–strain behaviour was modelled using the material model proposed by Kyprianou et al. [33], as expressed in Eq. (1). Where the input parameters are the Young's modulus E, the ultimate strength f_u, its corresponding strain ε_u, and n, controlling the roundness of the curve.

$$\varepsilon = \frac{\sigma}{E} + \left(\varepsilon_u - \frac{f_u}{E}\right)\left(\frac{\sigma}{f_u}\right)^n \tag{1}$$

Kyprianou et al. [34] demonstrated that the anisotropy of OSB, resulting from its manufacturing process, has a negligible effect on the response of the composite systems examined. Therefore, this study adopts the mean values of the mechanical properties in the longitudinal and transverse directions, as reported in [33] and presented in Table 1. The corresponding stress–strain relationship of the OSB material defined by Eq. (1) is indicated in Fig. 5.

4.1.2. WAAM and LMD steels

Fig. 6(a) shows the full range stress–strain constitutive model of WAAM normal-strength steel, developed by Huang et al. [35], which has been adopted herein. The parameters of this constitutive model were adopted from [18] based on machined coupons with a nominal thickness of 3 mm. These include the elastic Young's modulus, the yield stress, and the ultimate tensile stress, which were taken as E = 214500 MPa, f_y = 391 MPa and f_u = 485 MPa, respectively.

Fig. 6(b) shows the LMD constitutive model based on standard AISI 316L stainless steel powder. Unlike WAAM, there is currently no general constitutive model for LMD materials. However, given that the stress–strain response of LMD 316L stainless steel closely resembles that of conventionally manufactured steels, its nonlinear behaviour can be effectively captured using existing material models. As such, the generalised multistage formulation developed by Hradil et al. [36] was adopted, which has been calibrated by the tensile coupon tests conducted by Cacace et al. [37].

As can be observed, WAAM normal-strength steel and LMD stainless steel exhibit distinct mechanical characteristics due to differences in heat input, solidification patterns, and alloy composition. As reported by Huang et al. [18], WAAM-deposited normal-strength steel coupons show a well-defined yield plateau and strain-hardening behaviour similar to that of hot-rolled steels, as well as an almost isotropic mechanical response.

In contrast, LMD AISI 316L stainless steel exhibits a continuous and gradual transition from elastic to plastic behaviour, without a distinct yield point, and generally shows higher ductility than WAAM normal-strength steel. The experimental tensile data from the study by Cacace et al. [37] were adopted herein because their specimens were fabricated using the same LMD facilities and similar process parameters employed for the prototyping work described in Section 6. Their tensile tests were conducted in a single loading direction on printed specimens; therefore, an isotropic material model was used for the LMD material in the FE simulations.

4.2. Modelling of screw connections

There are two types of screw connections in the models: steel-to-steel and OSB-to-steel. The shear behaviour of screws connecting CFS steel elements, as used in joist-to-stud connections, was modelled using the general model proposed by Tao et al. [38]. The Eurocode [39] design equation for pull-out limit state was employed to determine the fastener capacity under tensile loading. To capture the shear and tensile limit states of self-drilling screws in OSB-to-steel connections, the predictive models developed by Kyprianou et al. [33] were utilised. Specifically, a modified and two single Ramberg–Osgood models were applied to predict the load-slip and pull-through responses, respectively. Further details on these models and the corresponding expressions can be found in [33].

Both steel-to-steel and OSB-to-steel screw connections were modelled using point-based Radial-Thrust fasteners from the Abaqus library [31], with a radius of influence equal to the screw thread radius.

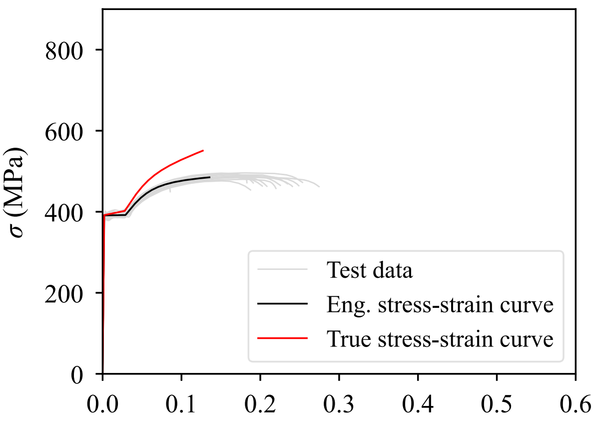

(a) WAAM

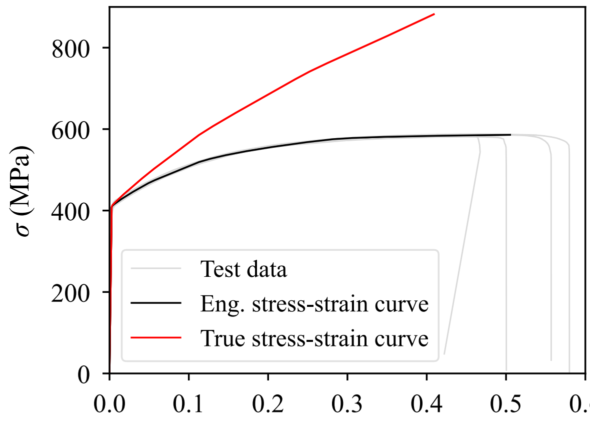

(b) LMD

Fig. 6. Stress–strain curves of AM materials.

Table 2
Mesh sensitivity analysis results for representative frame configurations.

Response parameter	SC3			GCW-42020			KCW-42020		
	Coarse	Medium	Fine	Coarse	Medium	Fine	Coarse	Medium	Fine
$V_{b,\max}$ (kN)	4.43	4.43	4.42	5.23	4.36	4.28	1.82	2.00	2.01
ULS analysis time (min)[a]	27	38	131	46	79	239	56	82	222
Deflection$_{\max}$ (mm)	10.55	10.57	10.60	11.60	11.62	11.73	13.39	12.35	11.97
SLS analysis time (min)	16	19	79	18	27	87	17	24	70

[a] Analyses were conducted using the Maxwell supercomputing cluster of the University of Aberdeen with 30 CPU cores (Intel(R) Xeon(R) Gold 6138 CPU @ 2.00 GHz) and 300 GB RAM.

The Radial and Thrust directions of the connector element correspond to the shear and axial load–displacement responses of the fasteners, respectively. Therefore, the connector's coordinate system is oriented such that these directions to be aligned with, and normal to, the contact surface of the two connected parts.

While point-based modelling of screw connections does not explicitly capture local failure mechanisms such as screw tilting, bearing, or thread interaction, the influence of these behaviours is implicitly represented through the calibrated force–displacement relationships of the fasteners in shear and tension [33,38]. Moreover, this approach significantly reduces computational cost compared to detailed three-dimensional modelling of individual screws while still providing reliable predictions of the global structural response of the connection.

4.3. Other specifications of FE modelling

The interaction between all parts was defined using the contact pair algorithm (*CONTACT PAIR) in Abaqus [31]. This includes contact between floor sheathing and joists, wall sheathing and studs, male and female connectors in GW connections, male connectors and joists in KW connections, joists and studs in screw and KW connections, and face track and studs. Master and slave surfaces were selected for each contact pair based on the relative thickness difference, where the thicker surface was defined as the master. Finite sliding was allowed, enabling arbitrary relative separation, sliding, and rotation of the contacting surfaces. For tangential behaviour, defined using a penalty formulation, a sensitivity study was conducted by considering friction coefficients of 0.2, 0.3, 0.4, and 0.5 for three representative frame configurations (SC3, GCW-42020, and KCW-42020). The joist mid-span deflection and base-shear capacity of the frames, representing the SLS and ULS responses, respectively, were evaluated and are presented in Appendix A, Fig. A.1. Based on the results, the SC3 frame showed negligible sensitivity to the friction coefficient because its response is governed primarily by the screw force–displacement behaviour. In contrast, the GW and KW frames exhibited increased base-shear capacity and reduced joist mid-span deflection with increasing friction coefficient, as expected, because their load transfer mechanism is governed by bearing and sliding interaction between the interlocking surfaces. Since higher friction coefficients led to increased structural resistance, a value of $\mu = 0.2$ was adopted herein, as it provides a conservative result and was previously employed by [41] for similar CFS connection systems. Normal behaviour was defined as "Hard" contact using a non-linear penalty formulation to prevent penetration between the interacting surfaces while allowing separation when tensile forces develop. The contact stiffness was calibrated through the modelling and taken as 5800 $^{\mathrm{N}}/_{\mathrm{mm}}$. Geometric imperfections were incorporated using an eigenvalue elastic buckling analysis in Abaqus [31]. The first buckling mode was employed to find the general shape of the governing buckling mode (local or distortional buckling). The mode shape was then scaled by the factors proposed by Schafer and Peköz [42] (0.34t and 0.94t for the local and distortional imperfections), depending on which mode shape is governed, to obtain the initial cross-sectional shape of CFS members.

All parts, including steel components and OSB, were modelled using general-purpose quadrilateral S4R shell elements in Abaqus [31]. A mesh sensitivity study was conducted to assess the influence of element size on the numerical response and computational efficiency. Three mesh densities were investigated for the representative frame configurations: coarse (15×15 mm for CFS members and 3×3 mm for AM connectors), medium (10×10 mm for CFS members and 2×2 mm for AM connectors), and fine (5×5 mm for CFS members and 1×1 mm for AM connectors). The sensitivity assessment considered both ULS and SLS by comparing the predicted base-shear capacity, joist mid-span deflection, and computational time. Table 2 displays the numerical responses obtained from the sensitivity analysis for ULS and SLS, and their corresponding curves are shown in Fig. A.2 in Appendix A.

The results showed that the SC3 frame exhibited negligible variation in both ULS and SLS responses across all mesh densities, while the

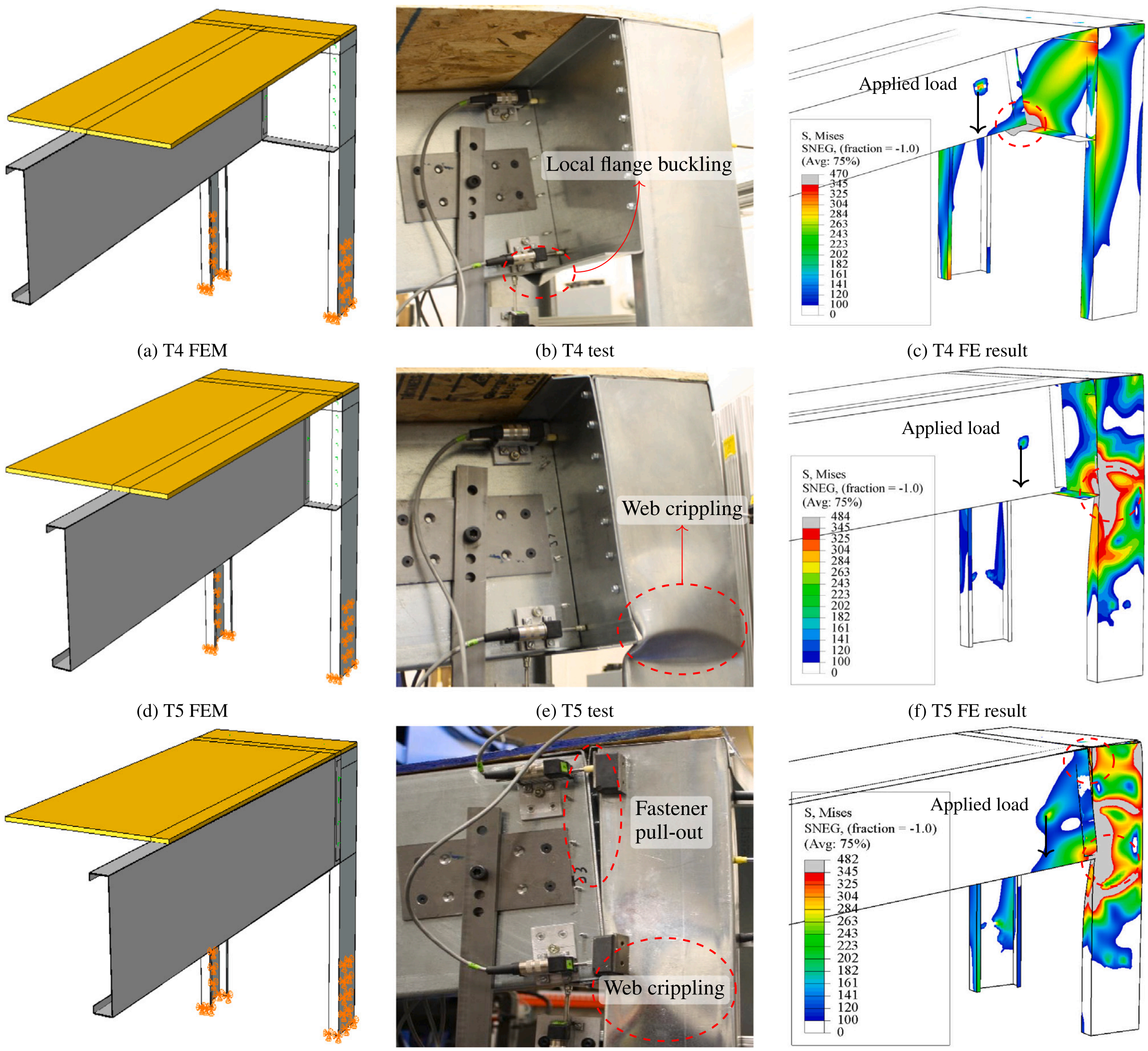

(a) T4 FEM (b) T4 test (c) T4 FE result

(d) T5 FEM (e) T5 test (f) T5 FE result

(g) T6 FEM (h) T6 test (i) T6 FE result

Fig. 7. Validation of the employed FE method.
Source: Experimental images were taken from [6,40].

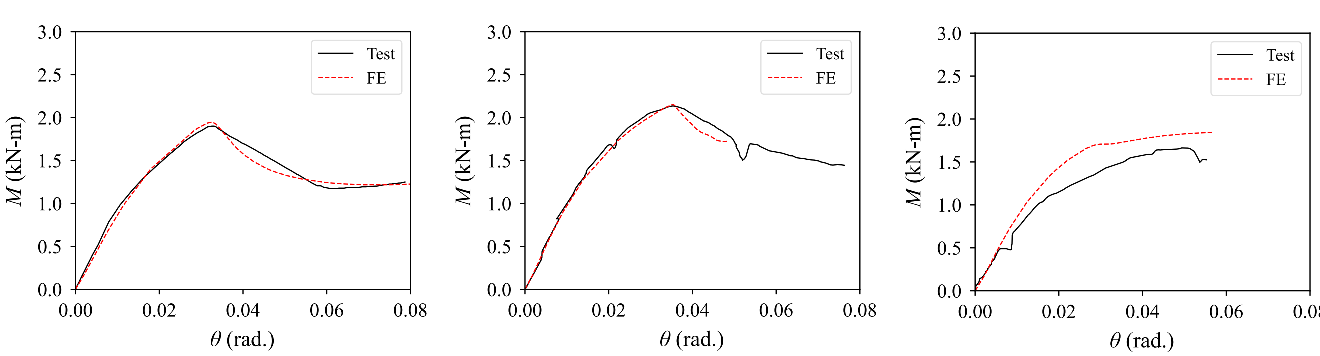

(a) T4 (b) T5 (c) T6

Fig. 8. Comparison of FE simulation and experimental test results of the ledger-framed system for moment–rotation response.

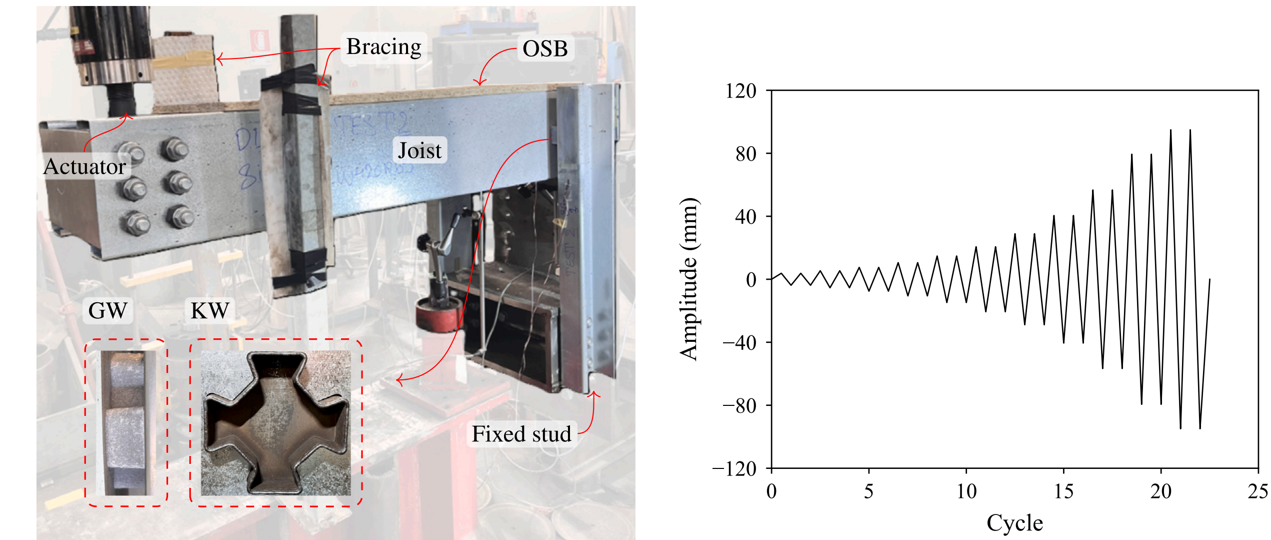

(a) Experimental test setup (b) Cyclic loading protocol [44]

Fig. 9. Structural-level test of AM-LSF system.

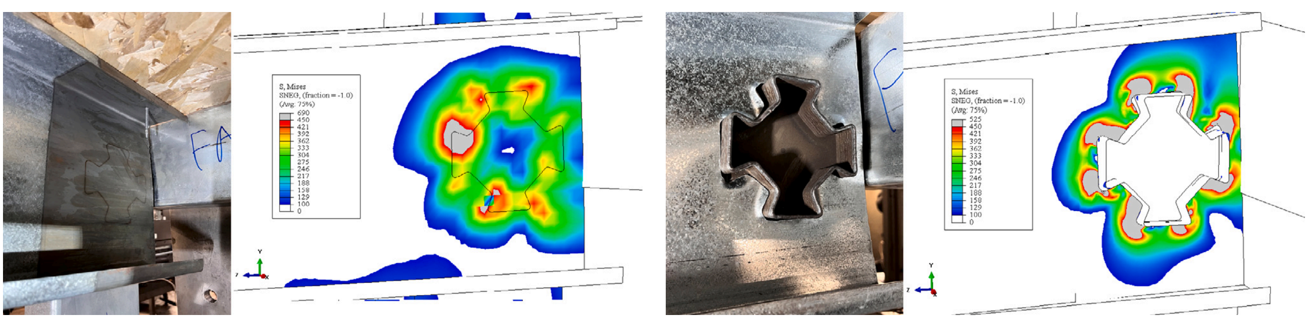

(a) GW connection (b) KW connection

Fig. 10. Validation of the FE method against the AM-LSF structural-level tests: experimental connection failure mode and FE stress distribution.

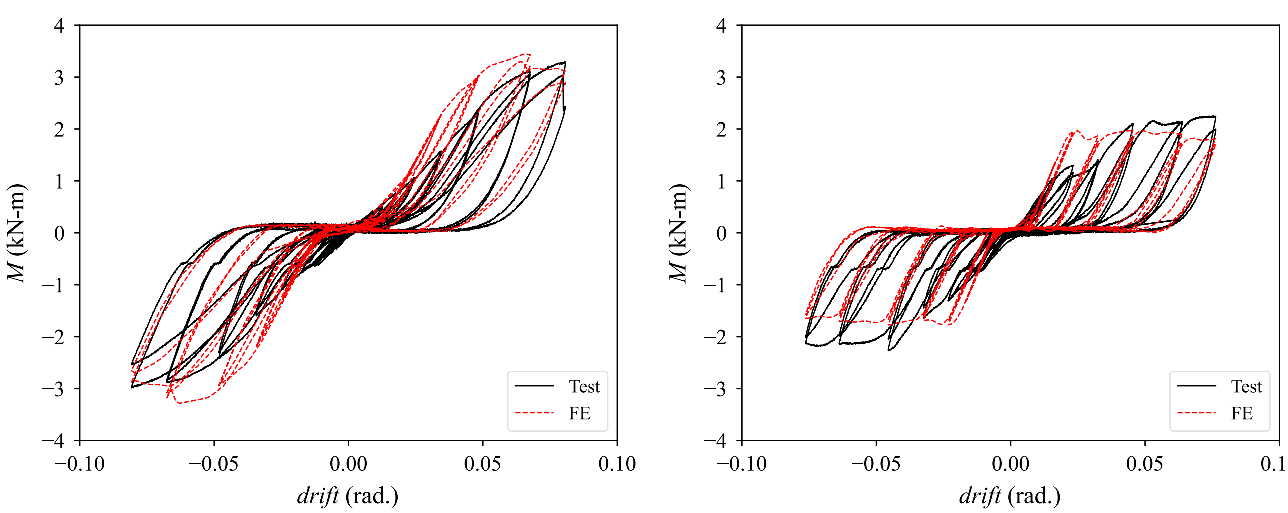

(a) GW connection (b) KW connection

Fig. 11. Comparison of FE and test cyclic moment–drift responses.

computational cost increased considerably with mesh refinement. For the GCW-42020 and KCW-42020 frames, the differences between the medium and fine meshes were less than 3% in terms of peak base-shear capacity and joist mid-span deflection, whereas the computational time for the fine mesh was about three times greater than that of the medium mesh. Based on these findings, mesh sizes of 2×2 mm, 10×10 mm, and 15×15 mm were adopted for the AM connectors, CFS members, and OSB components, respectively, as they provide an appropriate

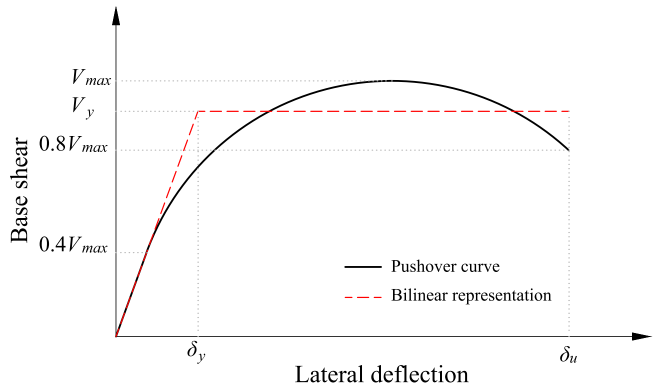

Fig. 12. Schematic representation of the EEEP method.

balance between computational efficiency and numerical accuracy. The FE analyses were conducted using the general static solver with artificial stabilisation, which has been successfully applied in previous studies [34].

4.4. Validation

The developed FE modelling approach was validated using two independent sets of experimental results: (i) existing ledger-framed connection tests from the literature [6], and (ii) two new structural-level tests carried out on AM-LSF assemblies with GW and KW connections and SCM [43].

4.4.1. Validation against ledger-framed connection tests

The FE model was first validated using the ledger-framed connection tests conducted by Ayhan and Schafer [6], which involve conventional screw connections in LSF systems. Among all tested specimens, T4, T5, and T6 were selected, representing different joist-to-ledger beam configurations; one with the joist positioned at the midpoint of the stud spacing, another placed adjacent to a stud, and the third directly on a stud. The modelling framework, including element type and size, contact interactions, connection fasteners, and analysis methodology, remains consistent with the FE model employed herein. The only difference was the incorporation of pull-out behaviour for steel-to-steel connections, which has been taken from the experimental results of Castaneda and Peterman [41]. In this study, the pull-out behaviour of the screw connections used in the ledger-framed connection tests conducted by [6] was experimentally investigated, making the results directly applicable for the present validation.

Fig. 7 presents the FE models of the three specimens together with the corresponding experimental test setups and the simulated failure modes. As can be observed, the FE simulations successfully capture the governing failure modes observed in the tests, including local flange buckling, web crippling, and fastener pull-out with web crippling for the T4, T5, and T6 specimens, respectively. Fig. 8 compares the moment–rotation responses obtained from the FE simulations with the corresponding experimental results for each connection configuration. As shown, the FE model provides close predictions of both the initial stiffness and the peak moment of the connections. The discrepancy observed between the FE and test results in Fig. 8(c) is about 10% in terms of peak moment. This difference is mainly attributed to the pull-out and pull-through behaviour of screws in the steel-to-steel and OSB-to-steel connections, respectively, which can introduce local variability in the connection response.

4.4.2. Validation against AM-LSF connection tests

To verify the applicability of the FE method to the proposed AM-LSF system, two structural-level tests, as shown in Fig. 9(a), were conducted on specimens incorporating GW and KW connections manufactured using LMD and WAAM processes, respectively. The assembly consisted of two 830 mm-long 150M14–75 stud walls spaced at 450 mm on centreline, fixed at the base and laterally restrained at the top using a 154M12–70 face track. Two 1350 mm-long 240M13–75 joists were connected to the studs through GSL42015 and KSW42033 connectors with a diameter of 110 mm in the GW and KW specimens, respectively. The connectors were fabricated using the same LMD and WAAM process parameters reported in Section 6. In the GW specimen an 18 mm OSB sheathing panel with dimensions of 1100 mm × 450 mm was installed on top of the joists using five #10 (4.8 mm) screws spaced at 250 mm, while the KW specimen was tested as a bare frame. The specimens were subjected to a cyclic loading protocol defined according to FEMA 461 [44], as shown in Fig. 9(b).

The von Mises stress distribution and the predicted structural performance are compared with the experimentally observed behaviour in Figs. 10 and 11, respectively. The global response is presented in terms of moment–drift behaviour, where drift is defined as the actuator vertical displacement normalised by the distance between the loading point and the connection centre. For the GW connection, as shown in Fig. 10(a), limited yielding occurred in the joist and wheel. In the KW specimen (Fig. 10(b)), the connector remained elastic, while the joist yielded around the wheel region, consistent with the experimental observations. The comparisons demonstrate reasonable agreement between the FE predictions and the experimental results, in terms of stress contours indicating local yielding around the wheels, as well as moment–drift response (see Fig. 11), including initial stiffness and peak moment. The difference between the FE predictions and the test results in terms of peak moment ranges between 4% and 12.5% for the two connection configurations. The FE input files used for the validation studies have been made available in the Data Availability section.

5. FE analysis results

Within this section, the results of the analysed frames with different connection configurations, as discussed in Section 3, are presented. At SLS the focus was on the deflection of the joists, while at ULS the base shear (V_b) of the frames, normalised by their seismic weight (W), based on EN 1998-1 [30], was evaluated against the lateral drift ratio (DR), defined as the ratio of the lateral storey displacement to the storey height.

The equivalent energy elastic–plastic (EEEP) method [45] was employed to idealise the nonlinear response of the frames under the ULS load combination. This method enables the evaluation of the frames' deformation capacity, defined in terms of the ductility factor (μ), and their energy dissipation capacity (E). As illustrated in Fig. 12, the idealisation process begins by drawing a line from the origin to the point corresponding to $0.4V_{max}$, where V_{max} is the maximum lateral capacity of the frame. A horizontal line then extends from the yield displacement (δ_y) to the ultimate displacement (δ_u), where the frame's load-carrying capacity drops by 20% from its maximum value. The yield point is determined such that the area under the bilinear approximation matches that of the nonlinear response curve, representing the energy dissipation capacity. Finally, the ductility factor is defined as the ratio of ultimate displacement to yield displacement ($\mu = \delta_u/\delta_y$).

The effects of connection type, construction method, printing materials, and the wheel geometrical parameters are presented as follows.

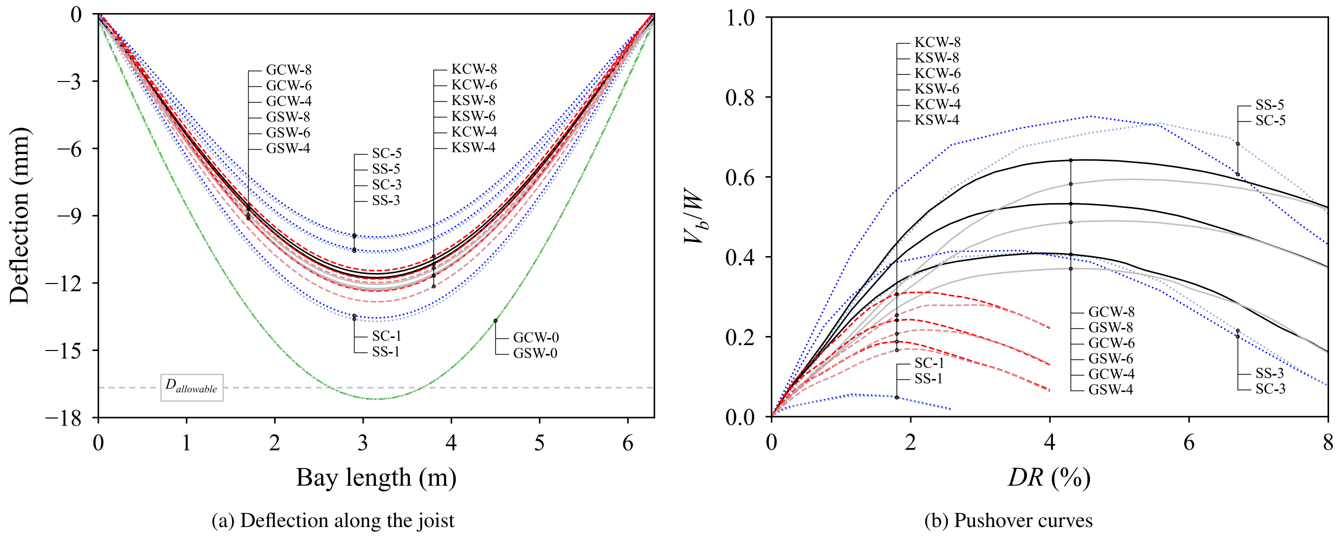

Fig. 13. Effect of connection type and construction method on (a) vertical deflection and (b) lateral drift. For AM connections: tooth depth = 20 mm; wheel thickness = 2 mm.

5.1. Effect of connection type and construction method

Fig. 13(a) and 13(b) show the vertical joist deflection along the bay length and the pushover normalised base shear versus lateral drift ratio response (V_b/W–DR) for various screw, GW, and KW connection configurations, shown in dotted blue, solid black, and dashed red line colours, respectively, with SCM and CCM (shown by lighter and darker lines, respectively). As expected, the frames with pin connections (GSW-0 and GCW-0 with round-shaped wheels) exhibited the largest mid-span deflections at SLS, exceeding the allowable $L/360$ limit [46], where L is the span length. In contrast, all the mid-span deflection of the semi-rigid frames remained within the acceptable limit.

For screw connections by increasing the number of screw lines from 1 to 5, the mid-span deflection was reduced by up to 27%. All the semi-rigid frames with GW and KW connections showed mid-span deflections between those of the frames with 1 and 3 screw lines, indicating their more consistent elastic connection stiffness at SLS. Moreover, across all the semi-rigid frames, regardless of the connection configuration, CCM frames (represented by darker colours) showed slightly lower deflections than their SCM counterparts. While this effect was minimal in screw connections, CCM frames with GW and KW configurations exhibited around 4% lower mid-span deflections than SCM frames.

Table 3 summarises initial stiffness K_0, maximum base-shear V_{max}, ductility factor μ, and energy dissipation capacity E, derived using the EEEP method discussed above, corresponding to the pushover curves presented in Fig. 13(b). On comparing the maximum of these values for each of the connection configurations, SC-5 showed 1.4 and 1.17 fold increase for K_0 and V_{max} than those of the GCW-8, while their E and μ values were close. Whereas, GCW-8 reached 4.8 and 2.1 times higher E and V_{max} than those of the corresponding KCW-8 frame, with K_0 and μ remaining in a similar range for both configurations.

As can be noticed for the screw connections, by increasing the lines of the screws from 1 to 5, K_0, V_{max}, and E were increased by around 3.4, 13.4 and 51 fold for CCM frames and similarly for SCM frames. While all the 4-tooth GW and KW connections (i.e., GSW-4, GCW-4, KSW-4 and KCW-4) outperformed the single line screw connections (i.e., SS-1 and SC-1), in terms of K_0, V_{max} and E values, the performance of SS-3 and SC-3 connections were comparable with those of the GSW-4 and GCW-4 connections. In general, regardless of connection type, CCM slightly outperformed SCM frames in terms of K_0, V_{max} and μ, while the E values for the corresponding CCM and SCM frames were in a close range. The improved performance of the CCM compared with the SCM can be attributed to the continuous vertical load path provided by the studs in the CCM, which reduces their effective length and increases the overall frame stiffness. As a result, the CCM frames show lower joist deflections at SLS and higher initial stiffness and lateral resistance in the pushover response at ULS.

Table 3
Pushover curve parameters of the semi-rigid frames presented in Fig. 13(b).

Connection label	K_0 (kN/m)	V_{max} (kN)	μ	E (J)
SS-1	31	0.55	3.7	25
SC-1	38	0.6	4.4	25
SS-3	78	4.36	3.3	586
SC-3	108	4.43	4.2	582
SS-5	86	7.83	2.7	1312
SC-5	127	8.01	3.5	1275
GSW-4	58	3.95	3.1	597
GCW-4	79	4.36	3.6	641
GSW-6	60	5.22	2.9	934
GCW-6	83	5.68	3.4	977
GSW-8	64	6.33	2.8	1276
GCW-8	89	6.85	3.4	1331
KSW-4	52	1.81	2.9	112
KCW-4	69	2.00	3.2	118
KSW-6	59	2.31	2.9	177
KCW-6	80	2.59	3.3	180
KSW-8	63	2.98	2.8	269
KCW-8	88	3.31	3.2	279

Fig. 14 shows the representative Von Mises stress contours of frames with SC-5, KCW-8, GCW-8, and GSW-8 connections corresponding to the ultimate displacement of the graphs presented in Fig. 13(b). For the frame with SC-5 connections (see Fig. 14(a)), screw shear failure was the dominant limit state, with corner screws taking the highest demand due to their greater distance from the connection centroid. In the frame with KCW-8 (see Fig. 14(b)), yielding of the joist bearing against the wheel area was the governing limit state, resulting in the modest performance, as discussed above, while both the wheel and stud remained elastic. For frames with GCW-8 and GSW-8 connections, as shown in Figs. 14(c) and 14(d), respectively, yielding of both male and female wheel connectors, along with localised yielding and buckling of the joist and yielding of the stud around the wheel areas, were the governing limit states, which led to the greater V_{max} and E values than those of the KW connections as discussed above.

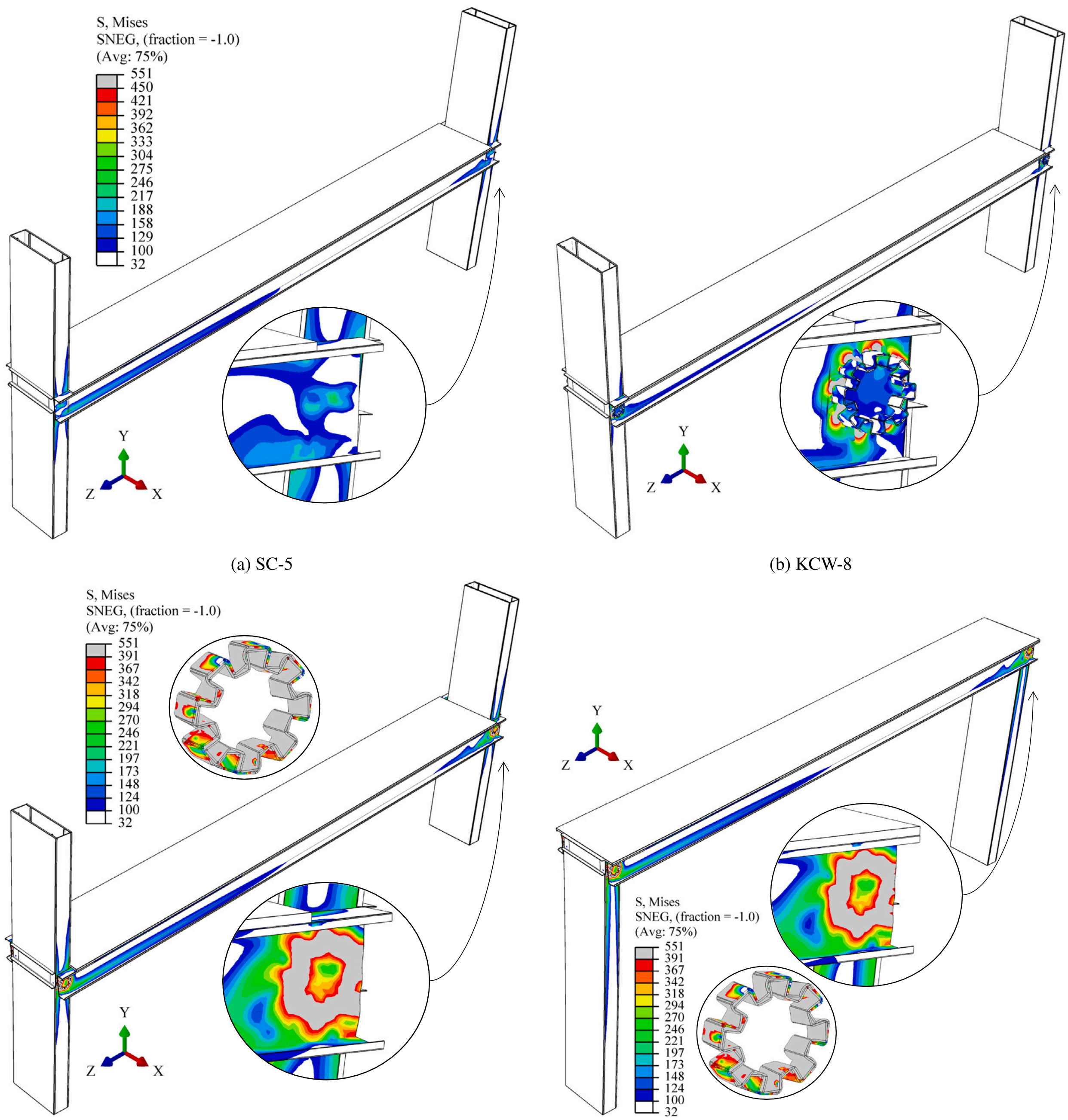

(a) SC-5 (b) KCW-8

(c) GCW-8 (d) GSW-8

Fig. 14. Von Mises contours for representative screw connection SC-5 and KCW-8, GCW-8 and GSW-8 AM connections.

5.2. *Effect of printing material*

Fig. 15 shows the effect of printing material, being WAAM and LMD shown by darker and lighter lines, respectively, on the joist deflection and the pushover response of CCM frames with 4-, 6-, and 8-tooth GW and KW connections. As can be seen, the joist deflection and the pushover curves of the KW connections were unaffected by changing the printing material. This is due to the governing limit state of the joist yielding of the KW connections, as discussed above. In contrast, for the frames with GW connections, WAAM-printed wheel connections led to a reduced mid-span deflection of 1.7% compared with those of the LMD-printed wheel connections. Furthermore, while K_0 of the WAAM-printed connections was higher by up to 5%, V_{max}, and E values were reduced by up to 7% and 11% than those of the LMD-printed connections. These results indicate that GW connections are affected by the material properties of the wheel connectors, owing to their dominant limit state involving yielding of both the male and female connectors, as discussed above.

5.3. *Effect of tooth numbers*

Figs. 16(a) and 16(b) illustrate the effect of tooth numbers on the response of CCM frames with 4-, 6-, and 8-tooth GW and KW connections. As expected, increasing the number of teeth from 4 to 8 resulted

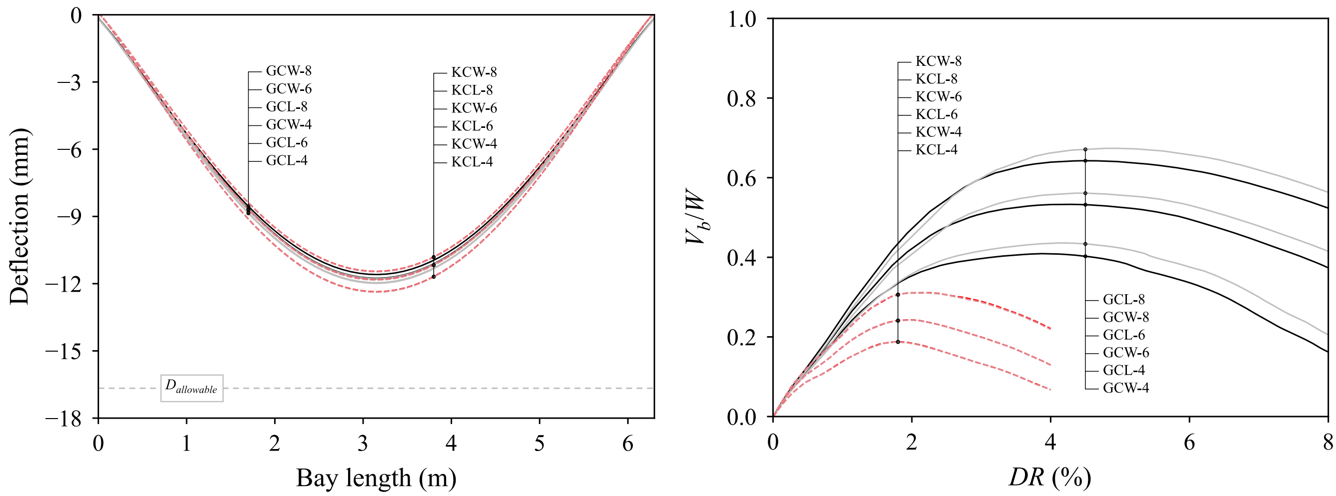

(a) Deflection along the joist

(b) Pushover curves

Fig. 15. Effect of printing material. For all connections: tooth depth = 20 mm; wheel thickness = 2 mm.

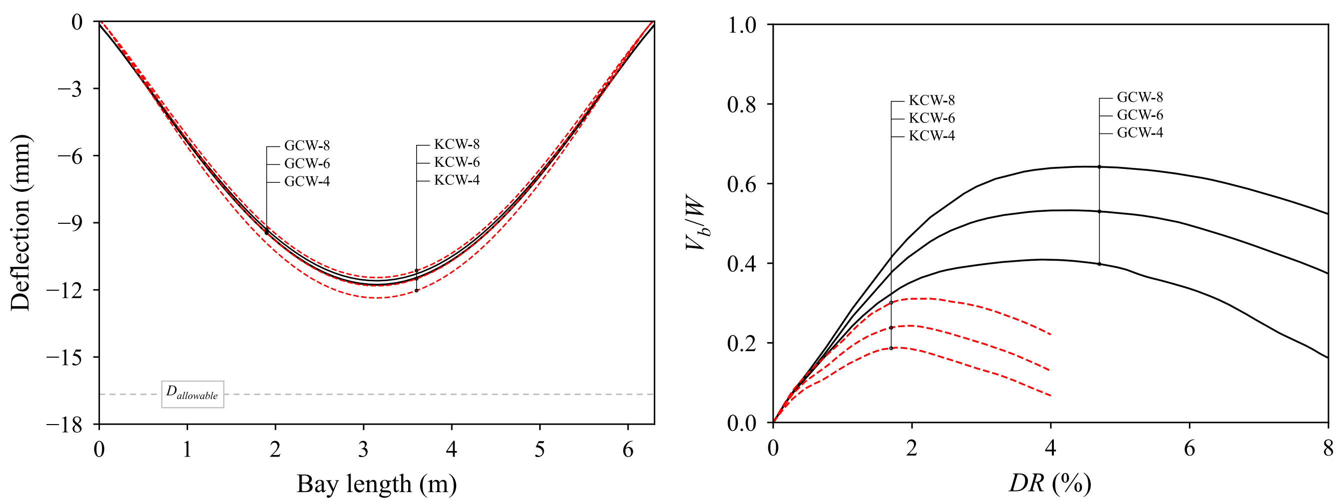

(a) Deflection along the joist

(b) Pushover curves

Fig. 16. Effect of tooth numbers. For all connections: tooth depth = 20 mm; wheel thickness = 2 mm.

in 1.8% and 7.6% reduction of mid-span deflection in the GW and the KW connections, respectively. In pushover response, GCW-8 and KCW-8 connections produced K_0, V_{max}, and E by 12%, 57%, and 108% and 28%, 65%, and 136% greater than those of the corresponding GCW-4 and KCW-4 connections, respectively. The improvement in structural performance with increasing tooth number can be attributed to the larger number of load transfer points between the male and female connectors in the GW configuration and between the wheel and the steel member in the KW configuration. This increases the effective contact area and distributes the bearing forces more evenly, thereby reducing local stress concentrations and improving the stiffness and load-carrying capacity of the connection. However, it is important to note that increasing the number of teeth results in higher heat input into the substrate, as discussed in Section 6.

5.4. Effect of tooth thickness

Fig. 17 shows the effect of tooth thickness of 1.5 mm and 2 mm (shown by lighter and darker lines) on the joist deflection and pushover response of CCM frames with 4-, 6- and 8-tooth LMD connections. As observed, the variation in tooth thickness had a negligible effect on both joist mid-span deflection and the pushover performance of frames with the KW connections. Conversely, increasing the thickness from 1.5 mm to 2 mm resulted in a reduction of joist mid-span deflection by up to 7.5% for GW connections. In the pushover response, the 2 mm thick GW connections exhibited increases of up to 1.4, 2.0, and 2.8 times in K_0, V_{max}, and E, respectively, compared with the corresponding 1.5 mm thick connections. The differing responses of the frames with GW and KW connections can be attributed to their governing limit states, as previously discussed.

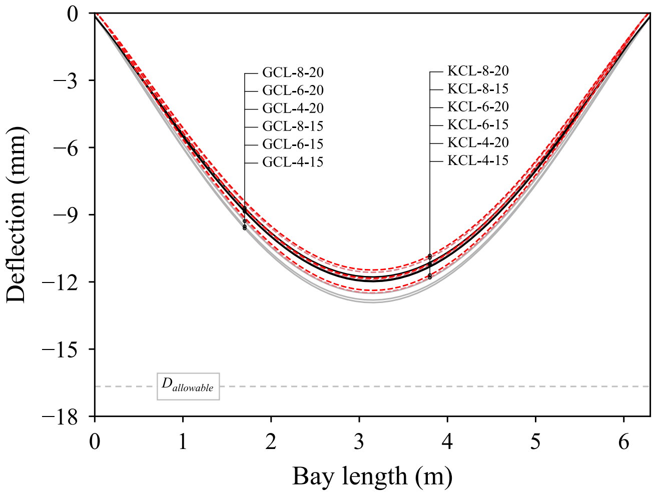

(a) Deflection along the joist

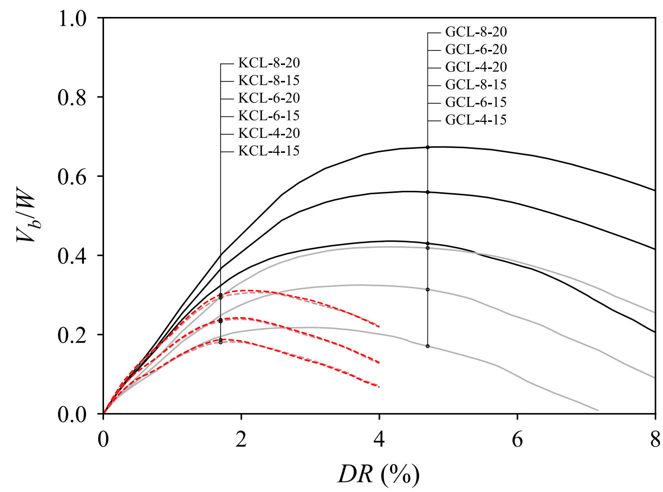

(b) Pushover curves

Fig. 17. Effect of tooth thickness. For all connections: tooth depth = 20 mm.

5.5. Effect of tooth depth

Fig. 18(a) and 18(b) show the effect of tooth depths of 20 mm and 40 mm (shown by lighter and darker lines, respectively) on the CCM frames with 4- and 6-tooth GW and KW connections. As observed, increasing the tooth depth resulted in up to 11% increase in mid-span deflection of the frames with GW connections, while this effect was negligible for the frames with KW connections. This highlights the difference of their interlocking mechanisms reducing the elastic stiffness of the GW frames by up to 40%. In terms of pushover response, increasing the tooth depth led to lower E and V_{max} by up to 29% and 33% for GW connections. In contrast, E and V_{max} were increased by up to 73% and 32% for the KW connections. This contrasting trend between GW and KW connections due to changes in tooth depth can be attributed to their distinct interlocking mechanisms. In the KW connections, increasing the tooth depth increases the interaction area between the joist and the wheel, thereby providing greater bearing resistance and yielding areas in the joists. Conversely, in the GW connections, a longer tooth depth results in a greater level of stress distribution along the depth of the wheel teeth, which in turn reduces the connection's stiffness, strength, and energy dissipation capacity.

6. Connection prototyping

To evaluate the printability of the proposed AM connection configurations and to identify potential challenges, extensive prototyping investigation was conducted in the laboratories of the Department of Mechanical Engineering at Politecnico di Milano, which hosts two state-of-the-art industrial robotic cells dedicated to additive manufacturing using WAAM and LMD. The WAAM cell is equipped with Cold Metal Transfer (CMT) technology integrated into a eight-axis robotic system, developed as part of the RocWAAM project for large-scale, automated metal part fabrication. The LMD cell, named AddiTube and provided by BLM Group, on the other hand, features a high-power laser and a powder feeding system, enabling precise deposition and production of components. While the full prototyping process will be reported separately, the featured solutions focused on both WAAM and LMD manufacturing methods are presented herein.

Male and female wheel connectors with 4-, 6-, and 8-tooth configurations, each having a radius of 55 mm and a tooth depth of 20 mm, were fabricated onto the webs of 250 mm-long substrates, cut from 150M14–75 and 240M16–75 sections, designed for the stud and joist, respectively. Prior to manufacturing, the zinc coating was stripped from the substrates using a 10% sulphuric acid solution to prevent the emission of harmful fumes and contamination of the AM material during welding. It should be noted that, in real practice, local re-coating (e.g., zinc-rich paint or equivalent protection) would be applied around the printed area after manufacturing to restore corrosion resistance. Furthermore, to minimise distortion during the printing process, a dedicated fixturing setup was employed, as shown in Fig. 19. The arrangement incorporated side plates to prevent lateral movement of the flanges, while a steel block together with top clamping plates provided out-of-plane restraint to the web, thereby improving the rigidity of the CFS substrate during deposition.

For the WAAM method, given the thin-walled nature of CFS substrates, a CMT welding process was adopted to minimise heat input and associated distortions. Stainless steel 316L feedstock wire with a 1.2 mm diameter was utilised for printing the wheels with calibrated process parameters summarised in Table 4. Note that the parameters used are those commonly adopted in industrial practice to minimise both the wall thickness of the wheel and the overall heat input. Regarding the adopted printing strategy, the wheels were printed with single passes by reversing the deposition direction in successive layers and changing the start and end points between layers. Furthermore, as the number of teeth increased, resulting in greater overall heat input, the inter-layer wait time was extended to allow adequate cooling of the substrate and mitigate heat-induced distortion. As shown in Table 4, dwell time of 2, 2.5, and 3 min were used for 4-, 6-, and 8-tooth wheels, respectively.

To address the geometric irregularities, including the hump at the start and the crater at the end of each deposited layer in CMT-based WAAM, as shown in Fig. 20(a), an improved start-end printing strategy based on [47] was adopted. To apply this strategy, the toolpath of each layer was initiated at the mid-point of a straight segment of the closed connector geometry (see Fig. 20(b)). Fig. 20(c) presents the corresponding toolpath parameters; a higher travel speed was applied at the start of each layer to reduce the deposited volume and limit hump formation. The travel speed was then gradually decreased in three steps to minimise the disturbance caused by the abrupt deceleration of the robot. At the end of each layer, an additional return path in the opposite direction (7.5 mm) was incorporated to fill the end-crater. As the start and end points coincide in a closed-loop path, a small

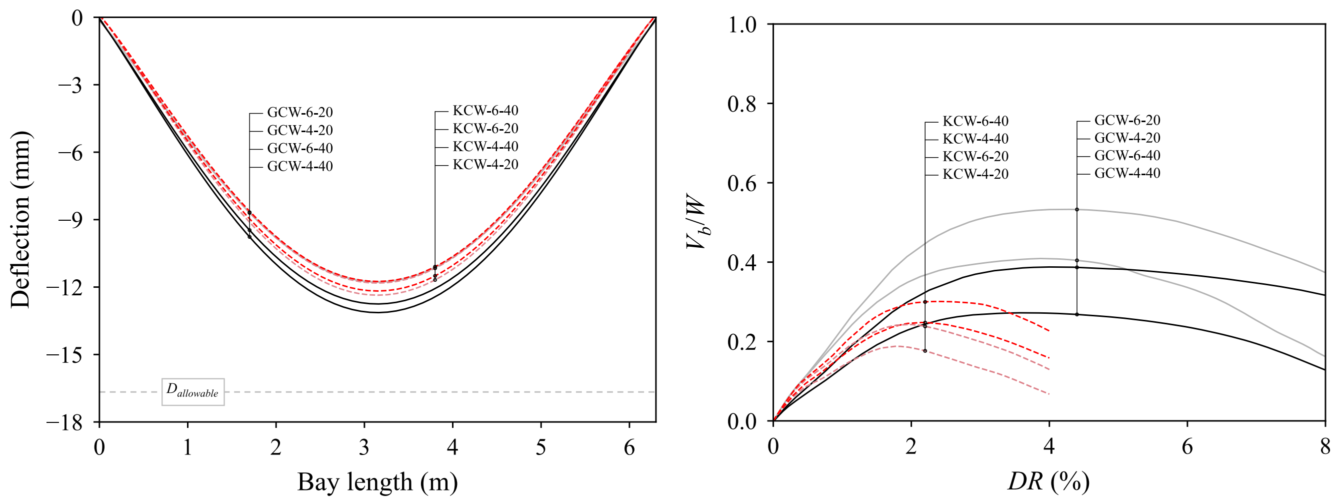

(a) Deflection along the joist (b) Pushover curves

Fig. 18. Effect of tooth depth. For all connections: tooth thickness = 2 mm.

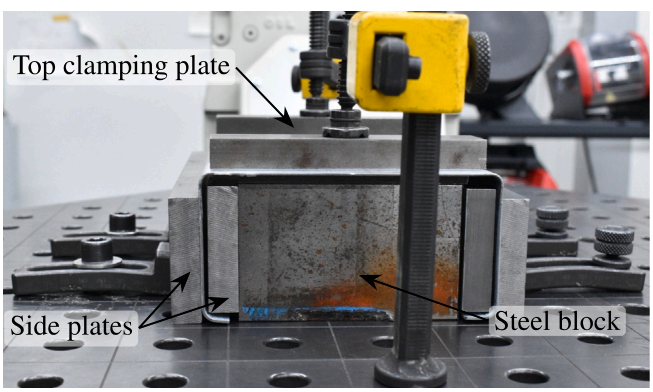

Fig. 19. Fixturing setup used during AM printing.

Table 4
WAAM process parameters.

Process parameters	Values
Wire feed rate (m/min)	1.5
Travel speed (mm/s)	5.5
Welding voltage (V)	9.7
Welding current (A)	58
Gas flow rate (L/min)	15
Welding mode	MIG CMT
Shielding gas	98% Ar + 2% CO_2
Dwell time (min)	2.0(2.5)(3.0)
Layer height (mm)	1.9

Table 5
LMD process parameters.

Process parameters	Values
Powder flow rate (gr./min)	8
Travel speed (mm/s)	18
Laser power (W)	400
Stand-off distance (mm)	8
Laser spot (mm)	1.2
Shielding gas flow rate (L/min)	15
Carrier gas flow rate (L/min)	5
Shielding gas	100% Ar
Layer height (mm)	0.3

intentional gap was introduced for the return path to avoid excessive material accumulation at the start of the layer. Because the return path was performed after a short cooling interval, a higher travel speed and a lower wire feed rate were used to prevent overheating and excess buildup at the layer end. The gap size, return-path length, the start travel-speed and wire-feed-rate values (shown in Fig. 20(c)) were calibrated through preliminary experiments.

The calibrated process parameters used for LMD printing are summarised in Table 5. Stainless steel AISI 316L powder was employed as the feedstock material. To ensure proper adhesion of the initial layers to the CFS substrate, a higher laser power of 420 W was applied for the first two layers of each connector. In contrast to the WAAM process, a continuous printing strategy without dwell time was adopted for LMD, owing to its significantly lower heat input. Moreover, a 0.5 mm clearance was considered for both WAAM and LMD between the maximum outer diameter of the male connector and the minimum inner diameter of the corresponding female connector to ensure proper interlocking for GW connections.

Figs. 21 and 22 illustrate the 4-, 6- and 8-tooth wheels along with a representative assembled 6-tooth GW connection printed by WAAM and LMD, respectively. As can be noticed, the wheels printed by LMD exhibited superior surface quality, minimal roughness, and more consistent and thinner wall thicknesses (ranging between 1.3–1.5 mm), with negligible substrate distortion. On the other hand, WAAM-printed parts had thicker teeth (3.2–3.7 mm), rougher surfaces, and a greater degree of substrate web distortion which could affect a precise assembly of the GW connections. This distortion was more pronounced in the joists than that of in the studs due to their larger web depth and reduced out-of-plane stiffness.

7. Concluding remarks

Within this research a hybrid lightweight structural system made of cold-formed steel (CFS) joist-stud framing incorporating novel, fastener-free, additively manufactured (AM) interlocking connections has been developed by means of validated finite element (FE) analyses and prototyping investigation. A comparative FE analysis at joist-stud

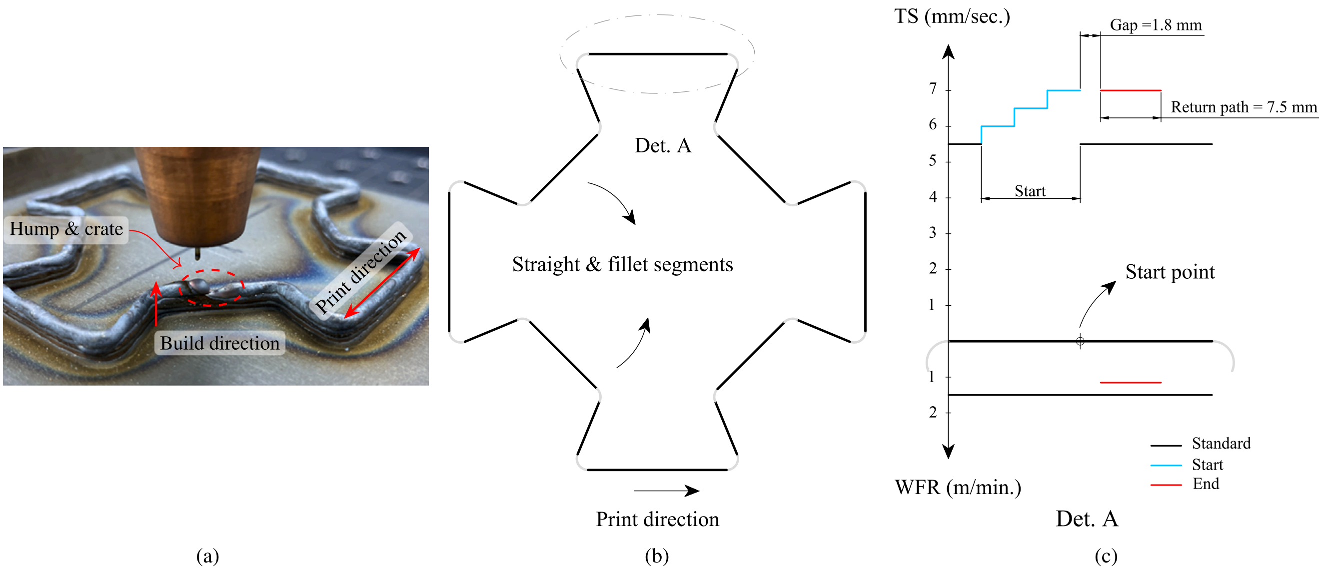

Fig. 20. Geometric irregularities in CMT-based WAAM deposition and the improved start–end printing strategy adopted to mitigate them: (a) typical start- and end-layer irregularities (hump and crater); (b) segments of the wheel connector; (c) calibrated toolpath parameters for the improved start-end strategy.

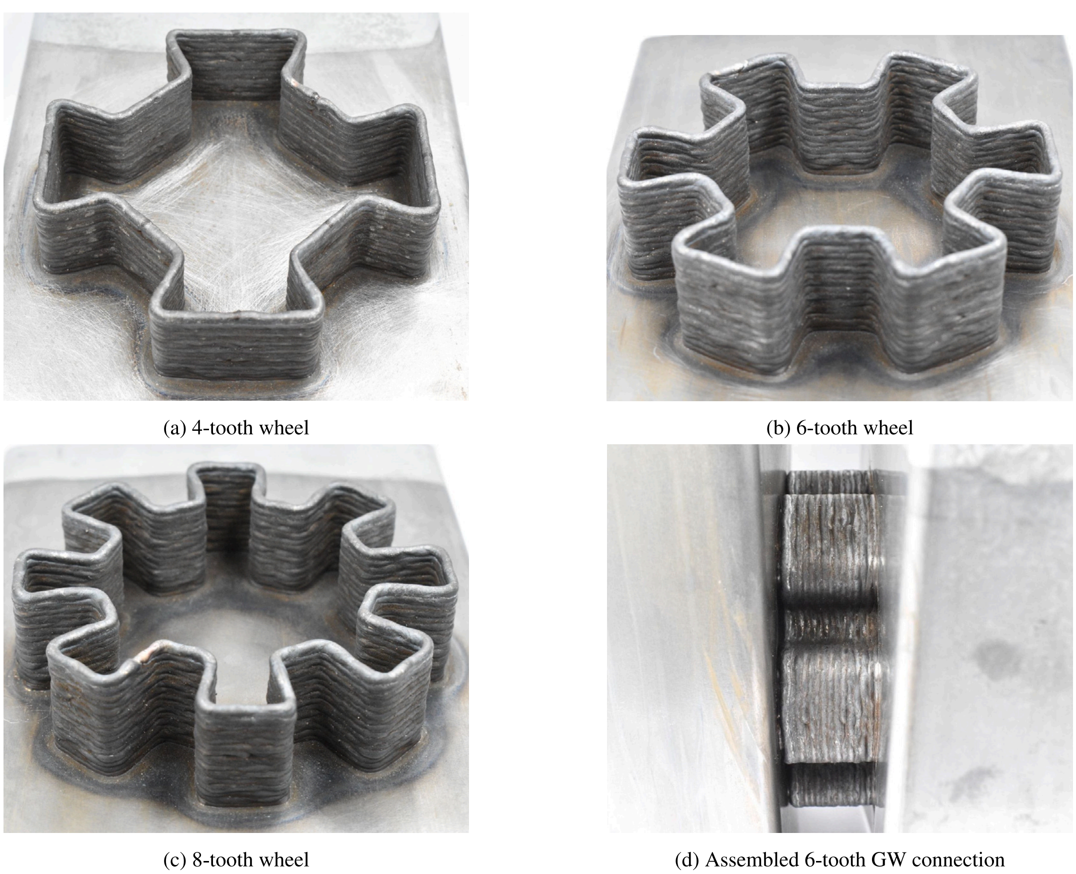

Fig. 21. 4-, 6-, and 8-tooth wheels and assembled 6-tooth GW connection printed using the WAAM process.

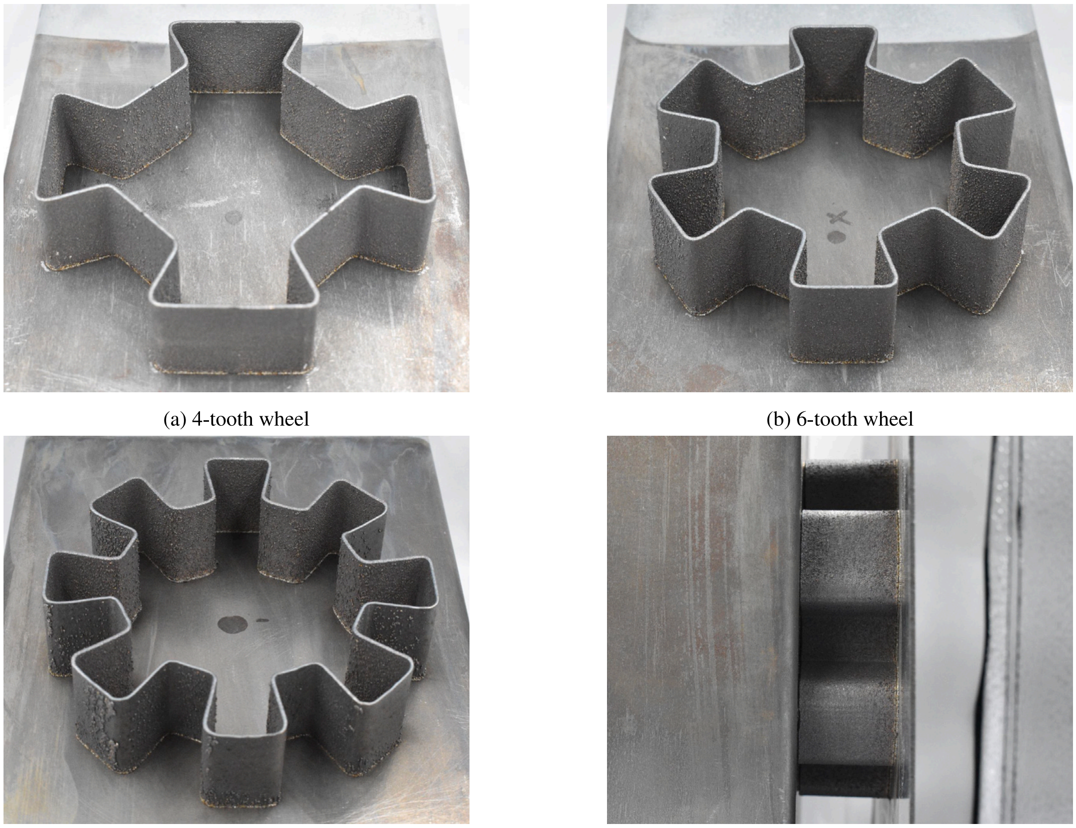

(a) 4-tooth wheel

(b) 6-tooth wheel

(c) 8-tooth wheel

(d) Assembled 6-tooth GW connection

Fig. 22. 4-, 6-, and 8-tooth wheels and assembled 6-tooth GW connection printed using the LMD process.

frame level was conducted incorporating two types of AM gear-wheel (GW) and key-wheel (KW) connection configurations, along with the conventional screw connection, considering both gravity and pushover loading conditions at serviceability and ultimate limit states (SLS and ULS), respectively. The AM connections comprised various 4-, 6- and 8-tooth wheels manufactured on both the joist and the stud for the interlocking GW connection, while for the KW connection the printed wheel on the stud interlocks with a matching hole in the joist. Effects of various parameters on the gravity and pushover responses of the frames were assessed, including connection type, construction method, being sequential (SCM) and continuous (CCM), printing material, including wire and arc additive manufacturing (WAAM) and laser metal deposition (LMD), and the wheel geometrical parameters. Vertical deflections under gravity loading along with pushover elastic stiffness (K_0), maximum base-shear (V_{max}), ductility factor (μ) and energy dissipation capacity (E) were extracted for each of the framing configurations. The key outcomes are as follows:

- While all the frames (except those with pin connections) satisfied the specified mid-span vertical deflection limit, the AM connections demonstrated a more consistent elastic connection stiffness compared with that of the screw connections.
- The pushover response of all the 4-tooth GW and KW connections outperformed the corresponding single line screw connections, while the performance of the 4-tooth GW connections was comparable with the three lines screw connections.
- As expected screw shear failure was the governing limit state of the screw connections, while a combination of joist–stud–wheel yielding due to a bearing action and local buckling of the joist around the connection region was identified as the governing limit state of the GW and KW connections.
- The LMD-printed GW connections slightly outperformed their WAAM-printed counterparts, whereas the performance of the KW connections was not affected by the printing material.
- Increasing the tooth numbers led to a reduced mid-span deflection and increased K_0, V_{max} and E values of both GW and KW connections, while increasing the tooth thickness had negligible effect on the performance of the KW connections.
- Increasing the tooth depth had contrasting effect on the performance of the GW and KW connections due to their different interlocking mechanism.
- AM connection prototyping of various wheel configurations revealed practical aspects related to WAAM and LMD methods, including dimensional accuracy, surface finish, and substrate distortion.

These findings lay the foundation for optimising connection designs to improve the overall structural efficiency of the proposed AM-LSF system. While the numerical models demonstrate predictive capabilities, the following future studies are recommended to further substantiate the results and support the practical adoption of the proposed system.

- Comprehensive experimental testing of the AM connection under cyclic, fatigue, and environmental actions (e.g., corrosion, humidity, and fire), including assessment of material anisotropy and thermally induced residual stresses.
- Development and evaluation of large-scale prototypes to validate system behaviour at structural level.
- Assessment of manufacturing tolerances and assembly procedures, as well as compatibility with existing design standards.

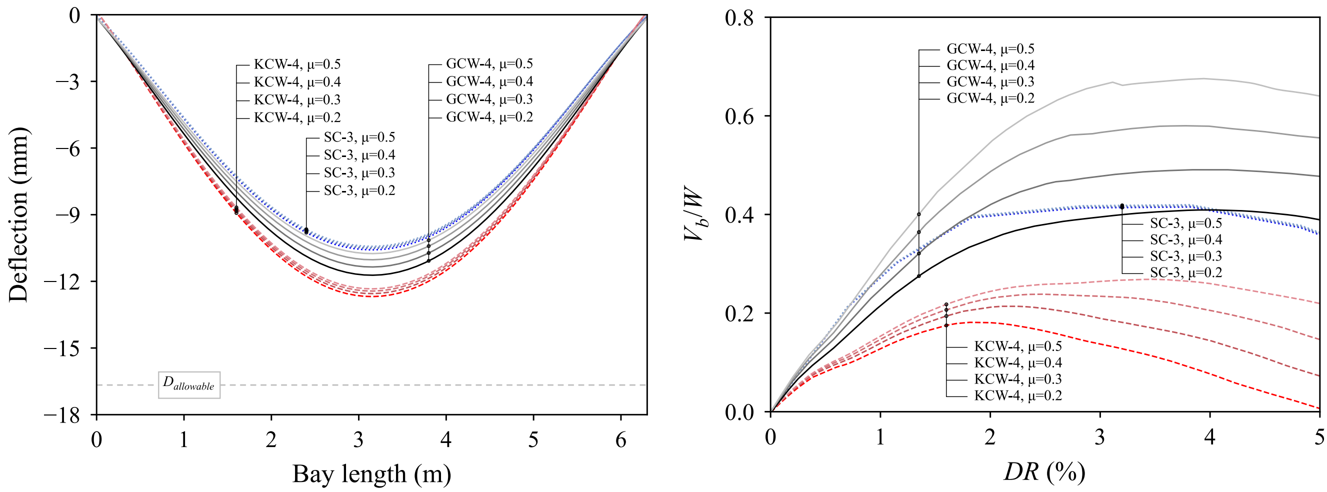

(a) Deflection along the joist (b) Pushover curves

Fig. A.1. Comparison of SLS and ULS responses obtained using different friction coefficients for the SC3, GCW-42020, and KCW-42020 frame configurations.

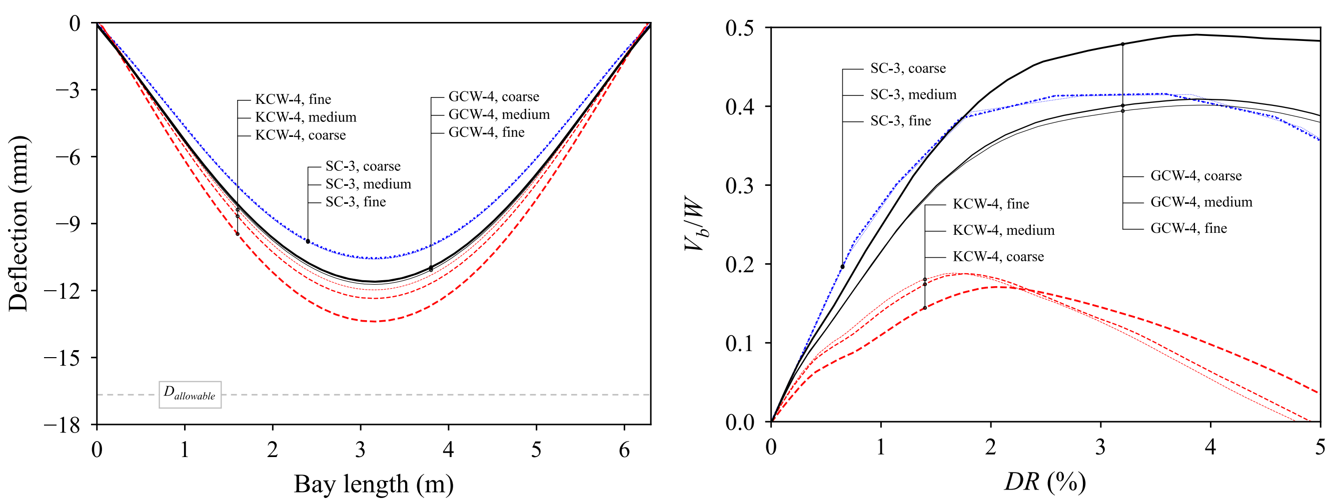

(a) Deflection along the joist (b) Pushover curves

Fig. A.2. Comparison of SLS and ULS responses obtained using different mesh densities for the SC3, GCW-42020, and KCW-42020 frame configurations.

- Economic assessment of AM-LSF system compared with conventional LSF systems.
- Investigation of sustainability aspects, including material efficiency, life-cycle impacts, and end-of-life scenarios.

CRediT authorship contribution statement

Ehsan Bakhshivand: Writing – original draft, Visualization, Validation, Software, Methodology, Investigation, Formal analysis, Data curation, Conceptualization. **Chuandong Xie:** Writing – review & editing, Validation, Software, Methodology, Investigation, Formal analysis. **Ornella Iuorio:** Writing – review & editing, Supervision, Project administration, Methodology, Investigation, Conceptualization. **Francesca Paradiso:** Writing – review & editing, Methodology, Investigation. **Barbara Previtali:** Writing – review & editing, Supervision, Project administration, Methodology, Investigation, Conceptualization. **Alireza Bagheri Sabbagh:** Writing – review & editing, Supervision, Project administration, Methodology, Investigation, Conceptualization.

Declaration of competing interest

The authors declare that they have no known competing financial interests or personal relationships that could have appeared to influence the work reported in this paper.

Acknowledgements

The connection developed in this paper is part of a filed patent application (No. 102025000010515, dated 09/05/2025). The authors would like to thank Prof. Luca Magagnin and Federico Lissandrello for their support with the zinc removal of the cold-formed steel sections. The 3D-printing and manufacturing support provided by Luca Tornaquindici and Akshay Ashok Benni is greatly appreciated.

The authors also acknowledge the AS_Lab at the Department of Architecture, Built Environment and Construction Engineering for hosting the research activities conducted during the research period in Milan. We also thank Metsec plc for supplying the prototyping and structural test sections. We are grateful to Giacomo Vazzana for the structural testing support, which was carried out at the Materials Testing Laboratory (LPM) of the Politecnico di Milano, grant 2025/1770. Additionally, the first author is grateful to the School of Engineering at the University of Aberdeen for funding his PhD.

Appendix A. Response curves for friction coefficient and mesh sensitivity analyses

Figs. A.1 and A.2 show the SLS and ULS response curves obtained from the friction coefficient and mesh sensitivity analyses conducted for the representative SC3, GCW-42020, and KCW-42020 frame configurations.

Data availability

The FE input files utilised for the validation study of AM-LSF systems have been made available in the following repository: ADDLIGHTS concept study.

References

[1] International Energy Agency, Tracking Industrial Energy Efficiency and CO2 Emissions, OECD, 2007, http://dx.doi.org/10.1787/9789264030404-en.
[2] L. Huang, G. Krigsvoll, F. Johansen, Y. Liu, X. Zhang, Carbon emission of global construction sector, Renew. Sustain. Energy Rev. 81 (2018) 1906–1916, http://dx.doi.org/10.1016/j.rser.2017.06.001.
[3] S.G. Maxineasa, D.N. Isopescu, I.-R. Baciu, M.L. Lupu, Environmental performances of a cubic modular steel structure: A solution for a sustainable development in the construction sector, Sustainability 13 (21) (2021) http://dx.doi.org/10.3390/su132112062.
[4] O. Iuorio, A. Gigante, R.F. De Masi, Life cycle analysis of innovative technologies: Cold formed steel system and cross laminated timber, Energies 16 (2) (2023) http://dx.doi.org/10.3390/en16020586.
[5] O. Iuorio, From mass prefab to mass customization: Modern methods of constructions from experimentation to manufacturing, in: SpringerBriefs in Applied Sciences and Technology, first ed., Springer, Cham, 2024, http://dx.doi.org/10.1007/978-3-031-73327-7.
[6] D. Ayhan, B. Schafer, Cold-formed steel ledger-framed construction floor-to-wall connection behavior and strength, J. Constr. Steel Res. 156 (2019) 215–226, http://dx.doi.org/10.1016/j.jcsr.2019.01.021.
[7] A. Bagheri Sabbagh, S. Torabian, Semi-rigid floor-to-wall connections using side-framed lightweight steel structures: Concept development, Thin-Walled Struct. 160 (2021) 107345, http://dx.doi.org/10.1016/j.tws.2020.107345.
[8] W. Gao, Y. Zhang, D. Ramanujan, K. Ramani, Y. Chen, C.B. Williams, C.C. Wang, Y.C. Shin, S. Zhang, P.D. Zavattieri, The status, challenges, and future of additive manufacturing in engineering, Computer-Aided Des. 69 (2015) 65–89, http://dx.doi.org/10.1016/j.cad.2015.04.001.
[9] D. Delgado Camacho, P. Clayton, W.J. O'Brien, C. Seepersad, M. Juenger, R. Ferron, S. Salamone, Applications of additive manufacturing in the construction industry – a forward-looking review, Autom. Constr. 89 (2018) 110–119, http://dx.doi.org/10.1016/j.autcon.2017.12.031.
[10] L. Gardner, Metal additive manufacturing in structural engineering – review, advances, opportunities and outlook, Structures 47 (2023) 2178–2193, http://dx.doi.org/10.1016/j.istruc.2022.12.039.
[11] S. Galjaard, S. Hofman, N. Perry, S. Ren, Optimizing structural building elements in metal by using additive manufacturing, in: Proceedings of IASS Annual Symposia, Vol. 2015, International Association for Shell and Spatial Structures (IASS), 2015, pp. 1–12.
[12] H. Strauss, E.P.P. AG, U. Knaack, Additive manufacturing for future facades: The potential of 3D printed parts for the building envelope, J. Facade Des. Eng. 3 (3–4) (2015) 225–235.
[13] C. Huang, X. Meng, L. Gardner, Cross-sectional behaviour of wire arc additively manufactured tubular beams, Eng. Struct. 272 (2022) 114922, http://dx.doi.org/10.1016/j.engstruct.2022.114922.
[14] L. Gardner, P. Kyvelou, G. Herbert, C. Buchanan, Testing and initial verification of the world's first metal 3D printed bridge, J. Constr. Steel Res. 172 (2020) 106233, http://dx.doi.org/10.1016/j.jcsr.2020.106233.
[15] ISO/ASTM 52900, Standard terminology for additive manufacturing technologies - general principles - terminology, Tech. rep., 2015.
[16] C. Buchanan, L. Gardner, Metal 3D printing in construction: A review of methods, research, applications, opportunities and challenges, Eng. Struct. 180 (2019) 332–348, http://dx.doi.org/10.1016/j.engstruct.2018.11.045.
[17] D. Svetlizky, M. Das, B. Zheng, A.L. Vyatskikh, S. Bose, A. Bandyopadhyay, J.M. Schoenung, E.J. Lavernia, N. Eliaz, Directed energy deposition (DED) additive manufacturing: Physical characteristics, defects, challenges and applications, Mater. Today 49 (2021) 271–295, http://dx.doi.org/10.1016/j.mattod.2021.03.020.
[18] C. Huang, P. Kyvelou, R. Zhang, T. Ben Britton, L. Gardner, Mechanical testing and microstructural analysis of wire arc additively manufactured steels, Mater. Des. 216 (2022) 110544, http://dx.doi.org/10.1016/j.matdes.2022.110544.
[19] V. Laghi, L. Arrè, L. Tonelli, G. Di Egidio, L. Ceschini, I. Monzón, A. Laguía, J.A. Dieste, M. Palermo, Mechanical and microstructural features of wire-and-arc additively manufactured carbon steel thick plates, Int. J. Adv. Manuf. Technol. 127 (3) (2023) 1391–1405, http://dx.doi.org/10.1007/s00170-023-11538-3.
[20] C. Buchanan, V.-P. Matilainen, A. Salminen, L. Gardner, Structural performance of additive manufactured metallic material and cross-sections, J. Constr. Steel Res. 136 (2017) 35–48, http://dx.doi.org/10.1016/j.jcsr.2017.05.002.
[21] J.-J. Yan, M.-T. Chen, W.-M. Quach, M. Yan, B. Young, Mechanical properties and cross-sectional behavior of additively manufactured high strength steel tubular sections, Thin-Walled Struct. 144 (2019) 106158, http://dx.doi.org/10.1016/j.tws.2019.04.050.
[22] C. Huang, X. Meng, C. Buchanan, L. Gardner, Flexural buckling of wire arc additively manufactured tubular columns, J. Struct. Eng. 148 (9) (2022) 04022139, http://dx.doi.org/10.1061/(ASCE)ST.1943-541X.0003427.
[23] X. Meng, B. Weber, M. Nitawaki, L. Gardner, Optimisation and testing of wire arc additively manufactured steel stub columns, Thin-Walled Struct. 189 (2023) 110857, http://dx.doi.org/10.1016/j.tws.2023.110857.
[24] J. Lange, T. Feucht, M. Erven, 3D printing with steel, Steel Constr. 13 (3) (2020) 144–153, http://dx.doi.org/10.1002/stco.202000031.
[25] S. Huang, X. Deng, L.K. Lam, Integrated design framework of 3D printed planar stainless tubular joint: Modelling, optimization, manufacturing, and experiment, Thin-Walled Struct. 169 (2021) 108463, http://dx.doi.org/10.1016/j.tws.2021.108463.
[26] X. Guo, P. Kyvelou, J. Ye, L. Gardner, Experimental investigation of wire arc additively manufactured steel T-stub connections, J. Constr. Steel Res. 211 (2023) 108106, http://dx.doi.org/10.1016/j.jcsr.2023.108106.
[27] X. Meng, J. Zhi, F. Xu, L. Gardner, Novel hybrid sleeve connections between 3D printed and conventional tubular steel elements, Eng. Struct. 302 (2024) 117269, http://dx.doi.org/10.1016/j.engstruct.2023.117269.
[28] X. Meng, L. Gardner, Hybrid construction featuring wire arc additive manufacturing: review, concepts, challenges and opportunities, Eng. Struct. 326 (2025) 119337, http://dx.doi.org/10.1016/j.engstruct.2024.119337.
[29] EN 1991-1-1, Eurocode 1: Actions on Structures, Part 1-1: General Actions-Densities, Self-weight, Imposed Loads for Buildings, no. 1-1, European Committee for Standardization (EN, Brussels, Belgium, 2002.
[30] EN 1998-1, Eurocode 8: Design of Structures for Earthquake Resistance, Part 1: General Rules, Seismic Actions and Rules for Buildings, no. 1–6, European Committee for Standardization (EN), Brussels, Belgium, 2004.
[31] Abaqus, Analysis user's manual, 2023.
[32] L. Gardner, X. Yun, Description of stress–strain curves for cold-formed steels, Constr. Build. Mater. 189 (2018) 527–538, http://dx.doi.org/10.1016/j.conbuildmat.2018.08.195.
[33] C. Kyprianou, P. Kyvelou, L. Gardner, D.A. Nethercot, Characterisation of material and connection behaviour in sheathed cold-formed steel wall systems – part 2: Analytical modelling, Structures 30 (2021) 1184–1199, http://dx.doi.org/10.1016/j.istruc.2020.12.052.
[34] C. Kyprianou, P. Kyvelou, L. Gardner, D.A. Nethercot, Finite element modelling of sheathed cold-formed steel beam–columns, Thin-Walled Struct. 183 (2023) 110365, http://dx.doi.org/10.1016/j.tws.2022.110365.
[35] C. Huang, P. Kyvelou, L. Gardner, Stress–strain curves for wire arc additively manufactured steels, Eng. Struct. 279 (2023) 115628, http://dx.doi.org/10.1016/j.engstruct.2023.115628.
[36] P. Hradil, A. Talja, E. Real, E. Mirambell, B. Rossi, Generalized multistage mechanical model for nonlinear metallic materials, Thin-Walled Struct. 63 (2013) 63–69, http://dx.doi.org/10.1016/j.tws.2012.10.006.
[37] S. Cacace, V. Furlan, R. Sorci, Q. Semeraro, M. Boccadoro, Using recycled material to produce gas-atomized metal powders for additive manufacturing processes, J. Clean. Prod. 268 (2020) 122218, http://dx.doi.org/10.1016/j.jclepro.2020.122218.
[38] F. Tao, A. Chatterjee, C.D. Moen, Monotonic and cyclic response of single shear cold-formed steel-to-steel and sheathing-to-steel connections, Technical Report CE/VPI-ST-16-01, Virginia Polytechnic Institute, Blacksburg, VA, USA, 2016.
[39] EN 1993-1-3, Eurocode 3: Design of steel structures, Part 1–3, :General rules - Supplementary rules for cold-formed members and sheeting, European Committee for Standardization (EN, Brussels, Belgium, 2006.

[40] D. Ayhan, Y. Qin, S. Torabian, B.W. Schafer, Characterizing joist-ledger performance for cold-formed steel light frame construction, in: Proceedings of the 8th International Conference on Advances in Steel Structures, ICASS, Lisbon, Portugal, 2015, pp. 22–24.

[41] H. Castaneda, K.D. Peterman, Moment–rotation response of cold-formed steel joist-to-ledger connections with variable-finishes in ledger-framed construction, J. Constr. Steel Res. 176 (2021) 106396, http://dx.doi.org/10.1016/j.jcsr.2020.106396.

[42] B. Schafer, T. Peköz, Computational modeling of cold-formed steel: characterizing geometric imperfections and residual stresses, J. Constr. Steel Res. 47 (3) (1998) 193–210, http://dx.doi.org/10.1016/S0143-974X(98)00007-8.

[43] C. Xie, A. Bagheri Sabbagh, E. Bakhshivand, O. Iuorio, Shape optimisation of metal additive manufacturing connections in lightweight steel structures, J. Constr. Steel Res. 241 (2026) 110290, http://dx.doi.org/10.1016/j.jcsr.2026.110290.

[44] Applied Technology Council, Interim testing protocols for determining the seismic performance characteristics of structural and nonstructural components, Tech. Rep. FEMA 461, Federal Emergency Management Agency (FEMA), Washington, D. C, 2007.

[45] American Iron and Steel Institute (AISI), North american standard for seismic design of cold-formed steel structural systems, S400-15 edition, Washington, D. C., 2015.

[46] International Building Code, International Code Council, Washington, D. C., 2021.

[47] Z. Wang, S. Zimmer-Chevret, F. Léonard, G. Abba, Improvement strategy for the geometric accuracy of bead's beginning and end parts in wire-arc additive manufacturing (waam), Int. J. Adv. Manuf. Technol. 118 (7) (2022) 2139–2151, http://dx.doi.org/10.1007/s00170-021-08037-8.